Tectonics®

RESEARCH ARTICLE
10.1029/2021TC007162

Key Points:

- The lower plate of East Humboldt Range metamorphic core complex, North American Cordillera, experienced significant attenuation
- Oligocene general shear zone decoupled from Miocene detachment faulting and regional extension
- Miocene-present extension and range tilting resulted in current exposure and geometry of this metamorphic core complex

Supporting Information:

Supporting Information may be found in the online version of this article.

Correspondence to:

A. V. Zuza,
azuza@unr.edu

Citation:

Zuza, A. V., Levy, D. A., Dee, S., DesOrmeau, J. W., Cheng, F., & Li, X. (2022). Structural architecture and attenuation of the ductile lower plate of the Ruby Mountain-East Humboldt Range metamorphic core complex, northeast Nevada. *Tectonics*, *41*, e2021TC007162. https://doi.org/10.1029/2021TC007162

Received 16 DEC 2021
Accepted 20 JUL 2022

Author Contributions:

Conceptualization: Andrew V. Zuza, Drew A. Levy
Data curation: Andrew V. Zuza, Joel W. DesOrmeau
Formal analysis: Andrew V. Zuza
Funding acquisition: Andrew V. Zuza, Seth Dee
Investigation: Andrew V. Zuza, Drew A. Levy, Seth Dee, Joel W. DesOrmeau, Feng Cheng, Xiangzhong Li
Methodology: Andrew V. Zuza, Joel W. DesOrmeau, Feng Cheng
Project Administration: Andrew V. Zuza, Seth Dee
Resources: Seth Dee, Xiangzhong Li
Software: Joel W. DesOrmeau
Supervision: Andrew V. Zuza, Seth Dee
Validation: Andrew V. Zuza
Visualization: Andrew V. Zuza

Structural Architecture and Attenuation of the Ductile Lower Plate of the Ruby Mountain-East Humboldt Range Metamorphic Core Complex, Northeast Nevada

Andrew V. Zuza[1], Drew A. Levy[1,2], Seth Dee[1], Joel W. DesOrmeau[2], Feng Cheng[3], and Xiangzhong Li[4]

[1]Nevada Bureau of Mines and Geology, University of Nevada, Reno, NV, USA, [2]Department of Geological Sciences and Engineering, University of Nevada, Reno, NV, USA, [3]Key Laboratory of Orogenic Belts and Crustal Evolution, Ministry of Education, School of Earth and Space Sciences, Peking University, Beijing, China, [4]Yunnan Key Laboratory of Earth System Science, Yunnan University, Kunming, China

Abstract Strongly deformed footwall rocks exposed in metamorphic core complexes (MCC) of the North American Cordillera were exhumed via ductile attenuation, mylonitic shearing, and detachment faulting. Whether these structures accommodated diapiric upwelling or regional extension via low-angle normal faulting is debated. The Ruby Mountains-East Humboldt Range MCC, northeast Nevada, records top-west normal-sense exhumation of deformed Proterozoic-Paleozoic stratigraphy and older basement. We conducted 1:24,000-scale mapping of the southwestern East Humboldt Range, with integrated structural, geochemical, and geochronological analyses to characterize the geometry and kinematics of extension and exhumation of the mylonitized footwall. Bedrock stratigraphy is pervasively intruded by Cretaceous, Eocene, and Oligocene intrusions, but observations of a coherent stratigraphic section show >80% vertical attenuation of Neoproterozoic to Ordovician rocks. These rocks are penetratively sheared with top-west kinematics. The shear zone thus experienced combined pure- and simple-shear (i.e., general shear) strain. We argue that this shear zone was syn-/post-kinematic with respect to Oligocene plutonism because: (a) mylonitic shearing spatially corresponds with preceding Oligocene intrusions; (b) thermochronology reveals that the shear zone experienced substantial cooling and exhumation after Oligocene plutonism; and (c) the mylonites are crosscut by undated, but likely late Oligocene, leucogranite. We propose that Eocene mantle-derived magmatism and thermal incubation led to Oligocene diapiric upwelling of the middle crust, with ductile stretching focused on the flanks of this upwarp. Regional Basin and Range extension initiated later in the middle Miocene. Therefore, the development of the East Humboldt Range shear zone was not driven by regional extension and coupled detachment faulting.

Plain Language Summary How the Earth's continental crust stretches and deforms is important for understanding how ancient mountain ranges collapsed in the past and how long these mountains can remain thick and elevated before they undergo the same fate. Regions known as metamorphic core complexes provide important windows into these processes, as they consist of strongly deformed and stretched rocks that were previously deeply buried. These rocks deformed at temperatures that were high enough for the rocks to slowly flow like a liquid. In this study, we mapped, dated, and examined rocks from the East Humboldt Range, northeast Nevada, to investigate exactly how these deeply buried rocks flowed during their migration toward the Earth's surface. Previous models argued that this geology resulted from extreme horizontal extension of the Great Basin over the past 30 million years. However, we interpret that these rocks only flowed locally due to doming of hot, lower crust rocks rising upward, over (geologically) brief timescales of several million years, about 29 million years ago. Therefore, the present-day extension in the Great Basin is not directly related to this older flowing process. Our interpretation emphasizes that hot crust can flow vertically, like hot wax convecting in a lava lamp.

1. Introduction

How metamorphic core complexes (MCC) accommodate strain and lead to high-magnitude displacement of upper plate vs. lower plate rocks is debated (e.g., Armstrong, 1982; Coney, 1980; Crittenden et al., 1980; Davis, 1983; Lister & Davis, 1989; E. L. Miller & Gans, 1989; Teyssier & Whitney, 2002). A general model for

Writing – original draft: Andrew V. Zuza
Writing – review & editing: Andrew V. Zuza, Drew A. Levy, Seth Dee, Joel W. DesOrmeau, Feng Cheng, Xiangzhong Li

MCC development involves regional extension that drives upper crustal stretching and exhumation of deeper rocks along ductile shear zones (e.g., Whitney et al., 2013), typified by low-angle normal fault models (e.g., Axen, 2020; Wernicke, 1981; Wernicke & Axen, 1988). However, localized crustal stretching may alternatively be driven by syn-kinematic intrusions leading to crustal diapirism, local crustal flow, and/or wallrock stretching around a plutonic margin (e.g., Konstantinou et al., 2012, 2013; E. L. Miller et al., 1983; Rehrig & Reynolds, 1980; Sylvester et al., 1978; Teyssier et al., 2005).

MCCs in the North American Cordillera have been intensely studied over the past half century, but disagreement exists about the timing, driving mechanisms, and magnitude of total lithospheric stretching and vertical thinning (e.g., Coney & Harms, 1984; Davis, 1983; Lister & Davis, 1989; E. L. Miller et al., 1983; Naruk et al., 1990; Wernicke, 1981). Our understanding of these systems and our ability to successfully restore their kinematic and thermal history back through geologic time is necessary to understand not just the mechanism of crustal extension, but also the Mesozoic convergent-margin history of the North American Cordillera, including the hypothesized Nevadaplano orogenic plateau (e.g., Coney & Harms, 1984; DeCelles, 2004). There is debate about whether the MCCs involve bulk non-coaxial vs. coaxial shear, which would correspond, respectively, to models of low-angle normal faulting with high-magnitude fault displacement vs. local crustal stretching, attenuation, and doming (e.g., Bailey & Eyster, 2003; Bartley & Wernicke, 1984; J. Lee et al., 2017; E. L. Miller et al., 1983; Platt et al., 2015). Kinematic, finite strain, and temporal observations across the ductile lower plate can potentially resolve between these end-member model scenarios.

In this work, we investigate the structural architecture and kinematic history of the mylonitic footwall a detachment fault (i.e., lower plate) in the Ruby Mountains-East Humboldt Range MCC, northeast Nevada (Figure 1), which exposes a complex record of Mesozoic contractional deformation, Mesozoic-Cenozoic intrusions, and Cenozoic extension (Snoke, 1980; Snoke et al., 1990). We focused on the top-west mylonitic shear zone that developed within the Proterozoic-Paleozoic paragneiss and voluminous Mesozoic-Cenozoic intrusions, located beneath the brittle detachment fault. We present new geologic mapping across the East Humboldt Range with U-Pb zircon dating of igneous and detrital samples, microstructural observations including electron backscatter diffraction (EBSD), geochemical analyses, and structural restoration to provide a viable kinematic history for the Cenozoic evolution of the Ruby Mountain-East Humboldt Range MCC. Our observations are consistent with a significant component of pure-shear ductile stretching of the upper-middle crust (E. L. Miller et al., 1983) that was later exhumed, and possibly reactivated, during later Miocene (post-17 Ma) detachment- and high-angle faulting active across the Great Basin (Colgan & Henry, 2009; Colgan et al., 2010).

2. Geologic Setting

The Ruby Mountain-East Humboldt Range exposes metamorphosed Proterozoic-Paleozoic paragneiss, lesser deformed upper Paleozoic sedimentary rocks, deformed Mesozoic-Cenozoic igneous rocks, minimally deformed (i.e., tilted) Miocene-present volcanic rocks, Cenozoic basin sediments, and Quaternary surficial deposits including several generations of glacial moraines (Howard, 1980; Snoke, 1980; Snoke et al., 1997, 1990; Snoke & Miller, 1988; Figures 1 and 2). The geologic history that most pertains to this study includes Neoproterozoic-early Mesozoic passive margin sedimentation on North American basement rocks, Mesozoic contractional deformation and magmatism, and Cenozoic magmatism and extension, described below.

Neoproterozoic-Paleozoic carbonate and siliciclastic passive margin rocks are exposed throughout much of northeastern Nevada (Figure 1). The total sedimentary thickness is 12–15 km (Bond et al., 1989; Hadlari et al., 2012; Stewart, 1972; Stewart & Poole, 1974). Passive margin sedimentation was partially interrupted by the Mississippian Antler orogeny, resulting in the deposition of Mississippian siliciclastic rocks (Beranek et al., 2016; Ketner, 2008; Poole & Sandburg, 1977; Speed & Sleep, 1982). This overall stratigraphy (discussed in the next section) is well resolved, which aids in reconstructions of the polyphase deformation in the region.

The Mesozoic geology of the region has been recently synthesized in Zuza, Henry, et al. (2021) and Zuza et al. (2020, 2022). The Ruby Mountains-East Humboldt Range region was in the Cordilleran retroarc, east of subduction along the western margin of the North American Cordillera (e.g., DeCelles, 2004; Dickinson, 2004). Middle-Late Jurassic intrusions, metamorphism, and southeast-directed shortening affected the region (Hudec, 1992; D. M. Miller & Hoisch, 1995; Thorman et al., 1991; Zuza, Henry, et al., 2021; Zuza et al., 2020), followed by Late Cretaceous metamorphism, anatexis with leucogranite intrusions, and shortening (e.g., Hallett

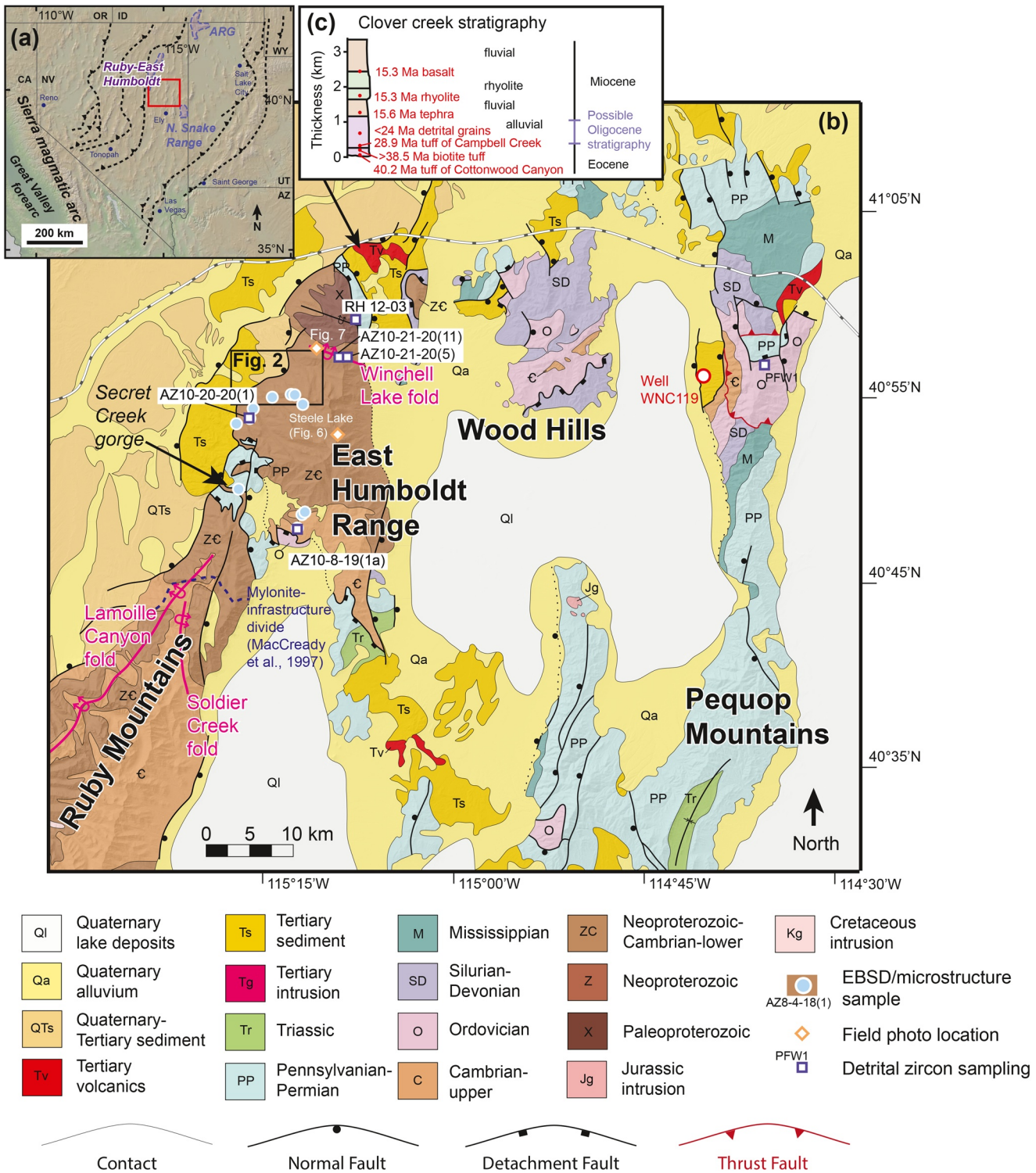

Figure 1. (a) Regional locator map of Cordilleran geology across Nevada, including the location of metamorphic core complexes and (b) in red. (b) Geologic map of northeast Nevada and northwest Utah, from the East Humboldt Range in the west to the Pequop Mountains in the east. Geology adapted mostly from Coats (1987), with modifications in the Pequop Mountains from Zuza, Henry, et al. (2021). Also shown are the locations of microstructural/EBSD samples (sample labels omitted for clarity but complete location information provided in Table 2), the detailed geologic map presented in Figure 2, and well WNC 119. (c) Simplified Clover Creek stratigraphy, showing available age constraints and only known, possibly Oligocene stratigraphy in the region (adapted from Zuza, Henry, et al., 2021). ARG, Albion-Raft River-Grouse Creek metamorphic core complex.

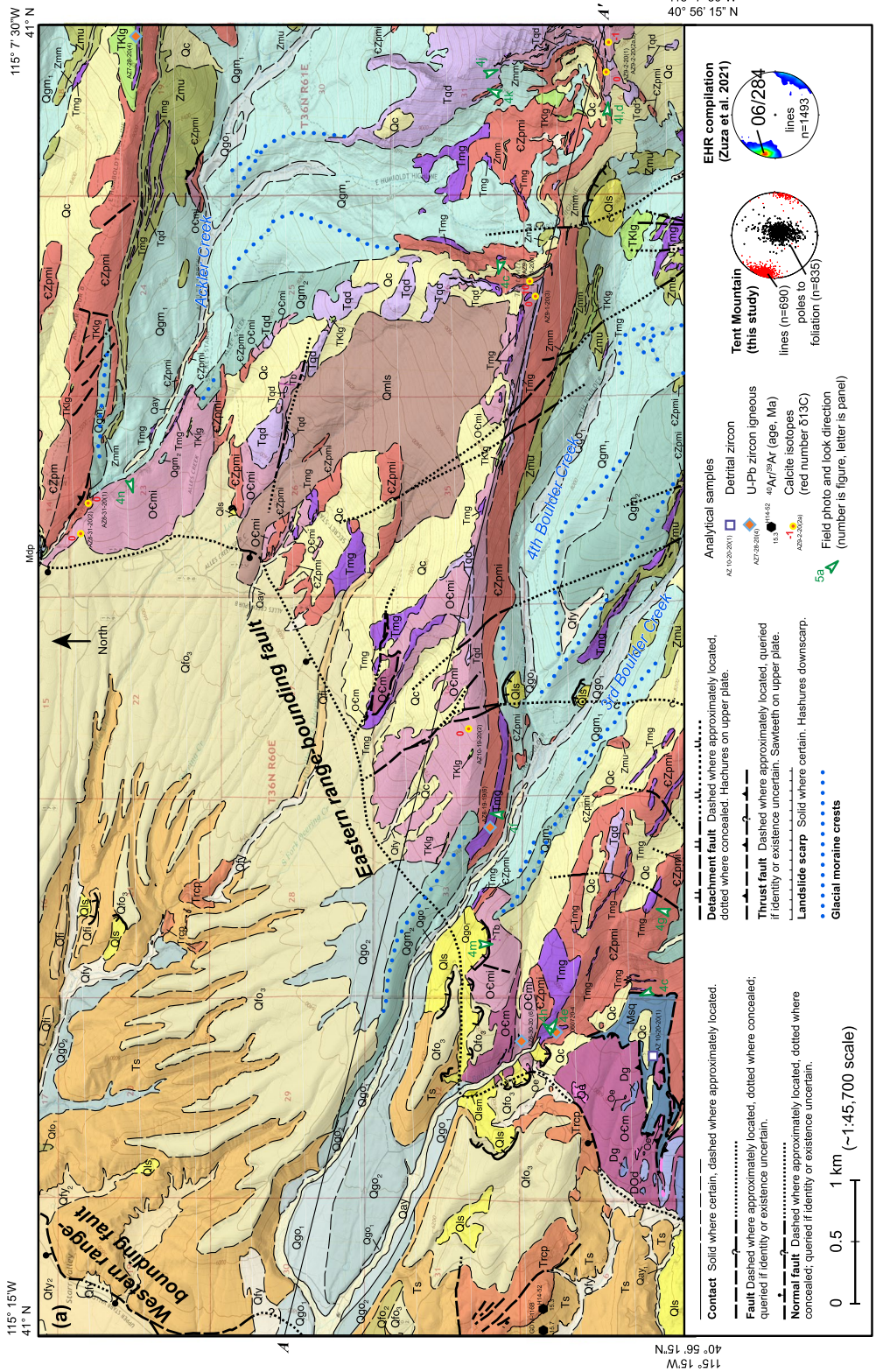

Figure 2. (a) Simplified geologic map of the northern half of the Tent Mountain quadrangle in the western East Humboldt Range, with geology based on 1:24,000-scale mapping of Hurlow (1987) and Zuza, Dee, et al. (2021). When drafted on a printed page, the scale was ~1:45,700 scale. Shown are the locations of samples discussed in this paper and field photographs. Some polygon labels removed for clarity. Note that most bedrock units are commonly intruded by >2/3 intrusions by volume but map units were defined based on discernible host-rock protolith. (b) Description of geologic units. (c) Geologic cross section across section A-A' from (a). Note that this profile was scaled 90% from panel (a).

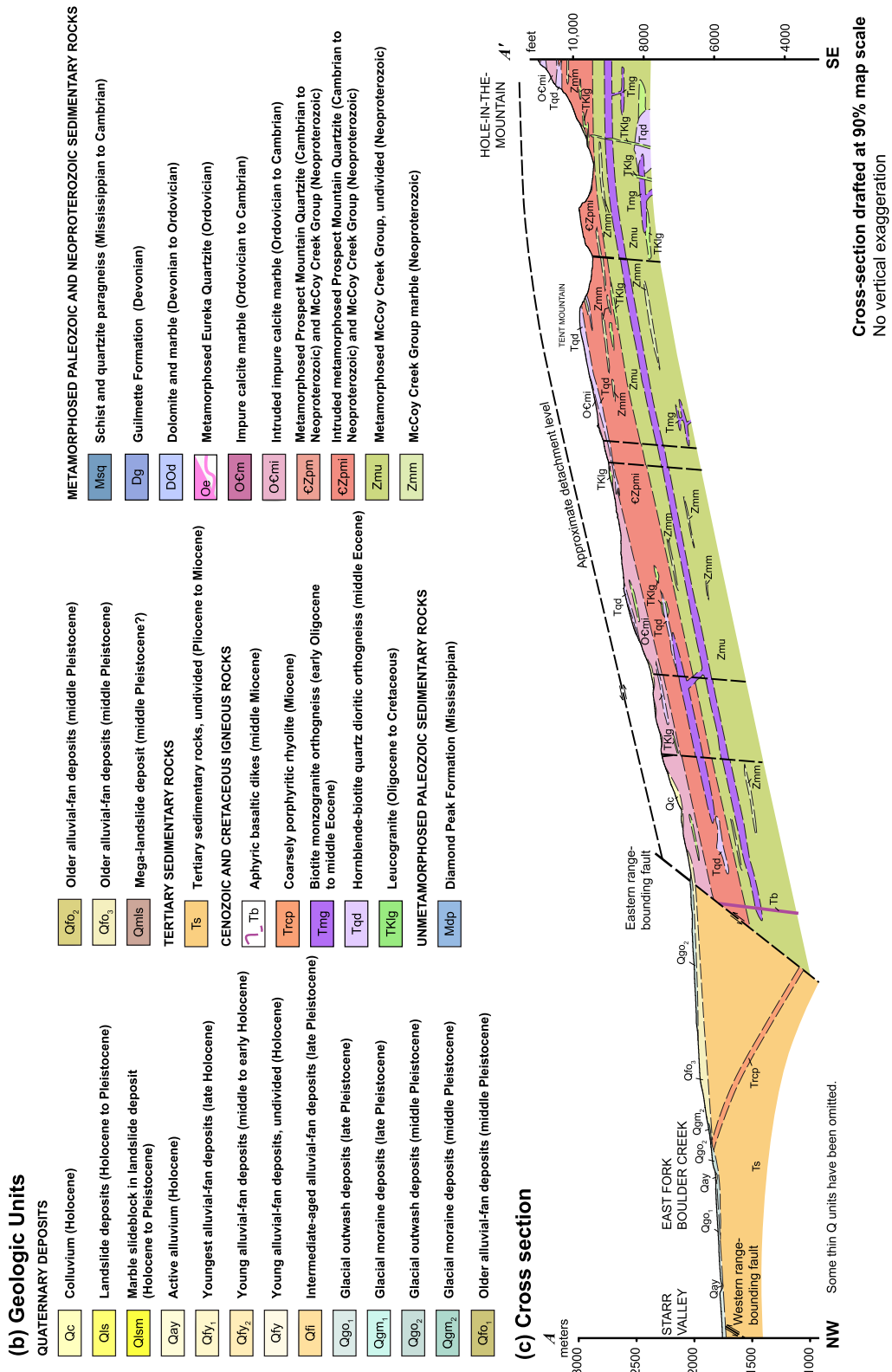

Figure 2. (Continued)

& Spear, 2014, 2015; S. Y. Lee et al., 2003; McGrew et al., 2000). Prograde metamorphism for samples from the East Humboldt Range reached peak pressures of 7–9+ kbar (Hallett & Spear, 2014, 2015; McGrew et al., 2000), although whether these pressures reflect lithostatic conditions and tectonic burial to 26–34+ km depths is debated (Thorman et al., 2019; Zuza, Henry, et al., 2021; Zuza et al., 2020, 2022). Compared to deformation in the Sevier fold-thrust belt to the east in central Utah (DeCelles & Coogan, 2006; Yonkee & Weil, 2015), Mesozoic shortening was more moderate ($\lesssim$30% strain), as evidenced by mapped contractional structures (e.g., Camilleri et al., 1997; Zuza, Henry, et al., 2021) and subcrop maps of the geology underneath Cenozoic unconformities (Konstantinou et al., 2012; Long, 2012; Van Buer et al., 2009). Various proxies support models where eastern Nevada was a relatively thick and high orogenic plateau by the end of the Cretaceous, including (a) structural reconstructions of extension (e.g., Coney & Harms, 1984; Long, 2019; McQuarrie & Wernicke, 2005) and contractional deformation (e.g., DeCelles & Coogan, 2006); (b) Sr/Y proxies (Chapman et al., 2015), (c) paleoaltimetry results (Cassel et al., 2014, 2018; Chamberlain et al., 2012), and (d) deeply incised east-flowing paleovalleys (e.g., Henry, 2008; Henry et al., 2011; Zuza, Henry, et al., 2021).

Late Cretaceous-early Cenozoic eastward shallowing of the Farallon slab has been interpreted to have resulted in Laramide deformation east of the Sevier belt (e.g., Axen et al., 2018; Copeland et al., 2017) and subsequent westward slab steepening starting in the Paleogene led to a southwestward sweep of magmatism across the Great Basin (e.g., Best et al., 2016; Cassel et al., 2018). In northeast Nevada, this was expressed by pervasive Eocene volcanism and intrusions observed in the Ruby Mountains-East Humboldt Range (Henry, 2008; Henry et al., 2012; Howard, 2003; Lund Snee et al., 2016). The Eocene Elko Basin (e.g., Lune Snee et al., 2016) also formed at this time, with subsidence potentially tied to Farallon slab dynamics (M. E. Smith et al., 2017). Next, an enigmatic phase of Oligocene plutonism affected the area, as evidenced by Oligocene granites observed in the Ruby Mountains-East Humboldt Range (Howard et al., 2011; MacCready et al., 1997; McGrew, 2018; McGrew & Snee, 1994; McGrew & Snoke, 2015; Wright & Snoke, 1993), which resulted in no reported volcanism (e.g., Lund Snee et al., 2016).

The extensional history of the Ruby Mountain-East Humboldt Range MCC is debated. Phases of Late Cretaceous-Eocene decompression are recorded via zircon and monazite dating and $^{40}Ar/^{39}Ar$ ages (Hallett & Spear, 2014, 2015; McGrew et al., 2000). This early phase of exhumation may reflect distributed ductile thinning of an eastward stretching thrust-fault hanging wall contemporary with shortening to the east in the Sevier thrust belt (Long & Kohn, 2020) or syn-to-post convergence normal faulting (e.g., McGrew et al., 2000). However, this kinematic history and chronology is hindered by a complicated thermal history and possible non-lithostatic pressure conditions for these highest grade rocks (Zuza et al., 2022, 2020). These models imply substantial exhumation on structures that have not yet been documented (see discussion in Hallett & Spear, 2015) or are strongly overprinted by middle-late Cenozoic extension and mylonitization. In this work, we refrain from interpreting this earlier phase of possible exhumation, but emphasize that the Late Mesozoic-Eocene structural and kinematic histories are poorly resolved.

Oligocene top-west mylonitization and unit attenuation is the most dominant structural feature of the East Humboldt Range (e.g., Hurlow et al., 1991; Snoke, 1980). Age constraints for this shearing are evidenced by the mylonitic shearing of Late Cretaceous, Eocene, and Oligocene intrusions, thus requiring some or all of this deformation after the emplacement of the youngest Oligocene deformed granites (e.g., Wright & Snoke, 1993). Hurlow et al. (1991) reported geothermobarometry results that suggest this mylonitization occurred at ~11–14 km depth (~3.1–3.7 kbar) and ~580°C–620°C. Age constraints for the cessation of mylonitization include fission track and $^{40}Ar/^{39}Ar$ biotite ages that record cooling through ~300°C–200°C by ca. 23 Ma (Dokka et al., 1986; McGrew & Snee, 1994; Wright & Snoke, 1993), which is below assumed temperatures for crystal-plastic quartz deformation and dynamic recrystallization (e.g., Stipp et al., 2002). Undeformed ca. 17–15 Ma basalt dikes, with chilled margins, cut the mylonites across the East Humboldt Range (Snoke, 1980; Zuza, Henry, et al., 2021), which provides another cross-cutting relationships for mylonitic shearing.

There are negligible records of Oligocene basin deposits (e.g., Lund Snee et al., 2016; Zuza, Henry, et al., 2021), which might be expected if Oligocene mylonitic shearing was coupled with regional detachment faulting during crustal extension (e.g., Dorsey & Becker, 1995; Friedmann & Burbank, 1995). The only known deposits that are *possibly* Oligocene are in the Clover Creek section (McGrew & Snoke, 2015), but refined geochronology suggests <500 m of strata could possibly be Oligocene (Zuza, Henry, et al., 2021; Figure 1c). However, these strata lack absolute dates and could be also Miocene.

Middle Miocene to present extension across northeast Nevada established the current range morphology (e.g., Colgan & Henry, 2009; Henry et al., 2011) and involved a phase of low-angle west-directed detachment faulting followed by later, high-angle normal faulting (Dokka et al., 1986; Haines & van der Pluijm, 2010; Hurlow, 1987; Snoke et al., 1990). Middle Miocene to present extension is associated with deposition of Miocene-present basins (Camilleri et al., 2017; Colgan & Henry, 2009; Henry et al., 2011; Zuza, Henry, et al., 2021), including deposition of the Miocene-Pliocene Humboldt Formation (Sharp, 1939; J. F. Smith & Ketner, 1978). Mapping and seismic data suggest that this sequence is up to 5 km thick in Lamoille Valley (Colgan et al., 2010; Satarugsa & Johnson, 2000). The Humboldt Formation was deposited after ca. 16 Ma based on $^{40}Ar/^{39}Ar$ dating and detrital zircon geochronology, with the basal tuffaceous sediments yielding a maximum depositional zircon age of ca. 24 Ma, although the base may be significantly younger (Lund Snee et al., 2016; Perkins & Nash, 2002; Wallace et al., 2008). In the Pequop Mountains to the east, Humboldt Formation sediments are exposed on the western flank of the range, where they are ≤2 km thick and well WNC 119 (Figure 1) suggests a local thickness ≤1 km (Zuza, Henry, et al., 2021). Ages for these sediments are as old as ca. 16 Ma (Camilleri et al., 2017; Zuza, Henry, et al., 2021).

3. Geologic Mapping in the East Humboldt Range

3.1. New Geologic Mapping

New geologic mapping in the East Humboldt Range was conducted in 2019–2021. Herein, we focus on 1:24,000-scale geologic mapping of the northern half of the Tent Mountain quadrangle (Zuza, Dee, et al., 2021), which was one of the last regions not previously mapped at such scale in the East Humboldt Range. Complete adjacent 1:24,000-scale quadrangle maps include Herder Creek to the north (Dee & Ressel, 2016), Welcome and Humboldt Peak to the northeast and east (McGrew, 2018; McGrew & Snoke, 2015), Gordon Creek to the southeast (Sicard & Snoke, 2021), Secret Valley to the south (Snoke et al., 2021), and Heelfly Creek to the west (Dee et al., 2015). The southern half of the Tent Mountain quadrangle was mapped as part of an M.S. thesis (Hurlow, 1987) and later by Zuza, Dee, et al. (2021). In this study, we also observed important regional structures in previously mapped regions, such as the Secret Creek gorge mylonitic shear zone and Winchell Lake nappe (e.g., Hacker et al., 1990; McGrew & Peters, 1997; McGrew et al., 2000).

3.2. Primary Geologic Units

The bedrock in the study area (summarized in a schematic column in Figure 3) consists of metamorphosed and mylonitized Proterozoic-Paleozoic sedimentary rocks, part of the passive margin sequence of western North America (e.g., Bond et al., 1989; Stewart, 1972; Stewart & Poole, 1974), and voluminous Cretaceous-Cenozoic igneous rocks. Unit divisions and correlations were based on earlier mapping of the East Humboldt Range (e.g., McGrew, 2018; McGrew et al., 2000; McGrew & Snoke, 2015; Sicard & Snoke, 2021; Snoke, 1980). The bedrock was commonly intruded by >2/3 intrusions by volume—observed at the outcrop and map scales—but we attempted to name map units by the host-rock protolith, following the approach used in the Ruby Mountains-East Humboldt Range since Howard (1966, 1971). This style of mapping may make the abundance of igneous intrusions in the map area appear less substantial than they actually are (Figure 2), but we reiterate that the igneous rocks are very extensive and dominate the bedrock exposures (e.g., Figures 3 and 4).

The oldest map unit is the Neoproterozoic McCoy Creek Group paragneiss (Zmu; Figure 3), which consists of pelitic schist, quartzite, and marble (Figures 4a–4d). The structurally deepest exposures of Zmu are commonly migmatitic (Figures 4c and 4d). Graphite-bearing white-gray calcite marbles within Zmu formed continuous and discontinuous layers that ranged in thickness from <1 to ~100 m, although most layers were <5 m (Figures 4j and 4l). When possible, the marbles were mapped separately as Zmm. Wickham and Peters (1993) demonstrated that the Neoproterozoic marbles display relatively high $\delta^{13}C$ values up to +12‰ (generally +6–10‰), whereas Paleozoic marbles yield $\delta^{13}C$ values closer to 0‰ or negative. In this study, we explored this observation further by conducting $\delta^{13}C$ analyses on marbles, and our results support this earlier observation. McCoy Creek Group rocks were differentiated from the overlying Neoproterozoic-Cambrian Prospect Mountain Quartzite due to the presence of interlayered and significant pelitic schist and marble layers. Prospect Mountain Quartzite is a relatively pure white quartzite. The Prospect Mountain Quartzite, Zmm, and Zmu were commonly mapped as a collective unit €Zpmi, due to relatively poor exposure, voluminous intrusions, and mylonitized and metamorphosed protolith rocks.

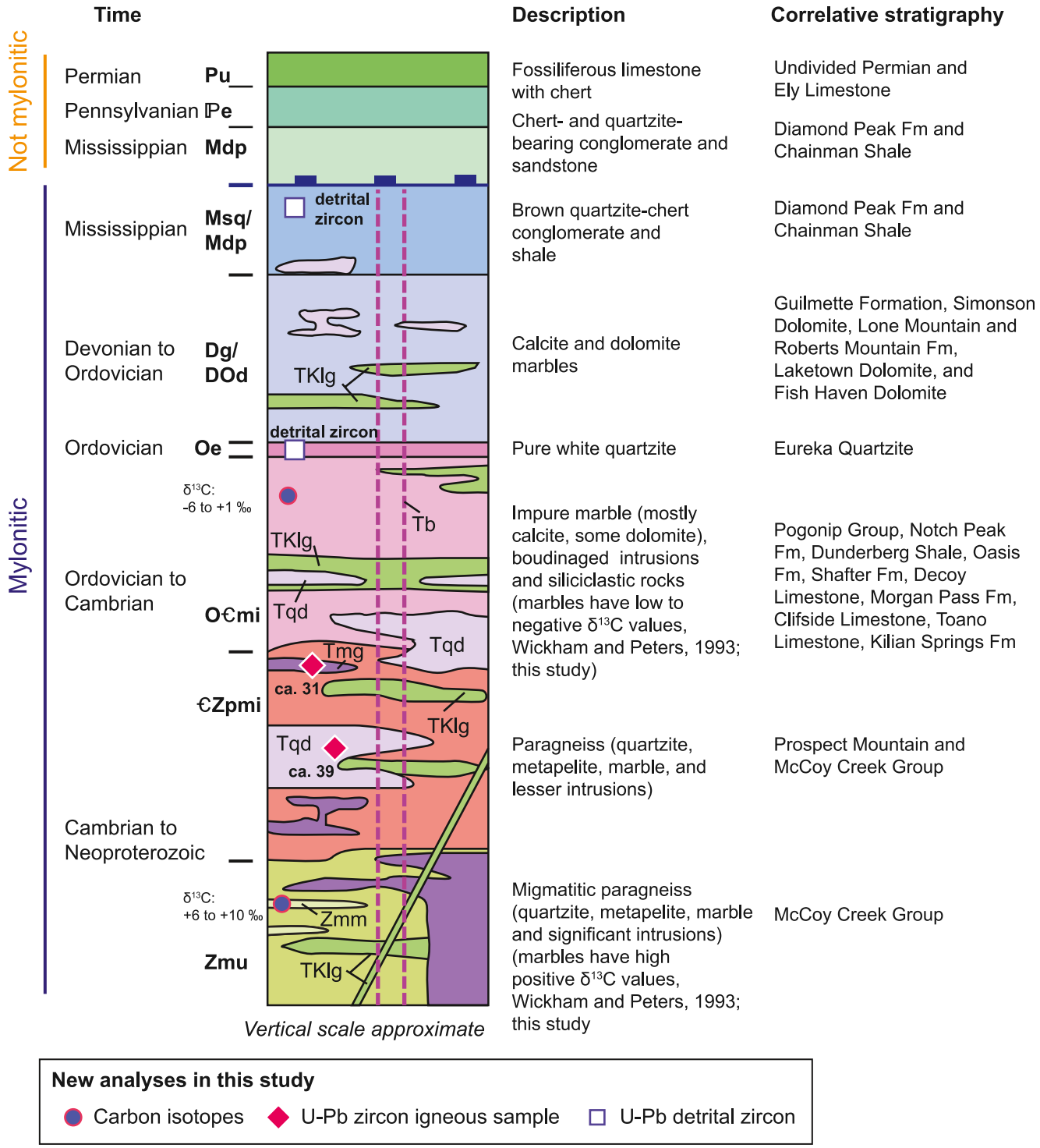

Figure 3. Interpretive stratigraphic column of the study area, displaying cross-cutting relationships, main rock types, and correlations with regional Neoproterozoic-Paleozoic stratigraphy.

Above €Zpm, the Cambrian-Ordovician impure marble sequence (O€m) consists of calcite marble, dolomite marble, calc-silicate rocks, and silty pelitic layers (Figure 3). The marbles are very diverse in their appearance, including color, foliation development, purity, and shearing. The lowermost part of unit includes highly folded siliciclastic and impure marble layers (Figure 4n). Boudinage of Cretaceous-Cenozoic igneous rocks (~1–50 cm

scale) in a flowing sheared marble matrix is commonly observed (Figure 4m), with a stretching direction parallel to the regionally observed ~WNW-trending lineation. Thin beds (<1 m) of pure-white quartzite, commonly discontinuous or expressed as lag on slopes, surrounded by marbles were interpreted as Ordovician Eureka Quartzite (Oe). The outcrop in Figure 5b shows an exceptional exposure of several meters of Oe, which was overlain by marbles and dolomite of the mixed Devonian-Ordovician marble and dolomite unit (DOd).

Less mylonitized, deformed, and intruded marbles were observed in a few locations in this map area, which we interpreted as structurally higher marbles faulted against higher grade marbles. These relationships were mapped as detachment fault slivers, similar to those of Hurlow (1987) in the southern Tent Mountain quadrangle. In the northernmost part of Figure 2 map, a rust-colored pebble conglomerate was interpreted as part of the Mississippian Diamond Peak Formation (i.e., Mdp). These rocks were faulted against mylonitic ЄZpmi quartzite. To the south in Secret Valley, Snoke et al. (2021) mapped Mdp as isolated klippe juxtaposed over OЄmi (Figure 5a). The rust-brown rock is very fine grained due to mylonitization, but streaky dark and light colors appear most similar to Mississippian Diamond Peak Formation, a distinctive conglomerate unit in eastern Nevada. New detrital zircon analyses discussed below support correlating Snoke et al. (2021)'s mapped Mdp unit with the Diamond Peak Formation.

A particularly poorly resolved map unit is a dark-brown carbonaceous schist and quartzite in the southwest corner of Figure 3, mapped as Msq. It is structurally above ЄZpmi quartzite and below mylonitic marble mapped as OЄm. This area has poor exposure on a dip slope, and thus robust structural relationships are ambiguous. We interpret these rocks as having a Mississippian clastic-rock protolith, and thus mapped it as Mississippian schist and quartzite (Msq) because it is rich in organic material, similar to the Mississippian Chainman Shale, and new detrital zircon data (this study) supports such a correlation.

In the southern Tent Mountain quadrangle, upper Paleozoic rocks (i.e., Mississippian through Permian limestone and shales) are detachment faulted above the strongly mylonitic units outlined above (Hurlow, 1987; Zuza, Dee, et al., 2021). The upper-plate stratigraphy is not intruded. Further discussion of the upper plate is outside the scope of the present study focused on lower-plate geology, and will be presented on in a future study.

Most sub-detachment paragneiss bedrock units are pervasively intruded by three igneous rock types: a Cretaceous-Tertiary leucogranite and leucocratic orthogneiss (TKlg), middle Eocene hornblende-biotite quartz diorite (Tqd), and Oligocene biotite monzogranite orthogneiss (Tmg). These intrusions commonly comprise a majority of the bedrock exposures, with Cenozoic Tmg and Tqd representing the greatest volume in the study area. The TKlg unit is commonly a weakly foliated two-mica leucogranite (±garnet). TKlg commonly forms discontinuous meter to sub-meter scale concordant sheets, pods or lenses throughout the rocks in the MCC. At deeper structural levels, minor leucogranite pods are surrounded by restitic biotite-sillimanite schist. Most leucogranite ages are Late Cretaceous, including ca. 85 Ma zircon ages (McGrew et al., 2000) and ca. 80 Ma U-Pb monazite ages (Hallett & Spear, 2015). Observations of TKlg intermingled with, or directly cross-cutting, the Cenozoic Tqd and Tmg intrusions (Figures 4c and 4d) require that the TKlg age range extends to as young as Oligocene. Therefore, the broad TKlg unit likely has a Late Cretaceous phase and an Oligocene phase that can be revealed by more systematic geochronology (e.g., Howard et al., 2011).

The Tqd unit is weakly to strongly foliated and lineated, and has a porphyritic texture with 1–2 mm plagioclase and lesser hornblende, biotite, and quartz. Tqd forms dark gray-black, jagged, high-relief cliffs that commonly define ridges (e.g., Figure 4i). It is less strongly foliated and lineated (Figure 4h), probably due to the relative strength of this more mafic igneous unit. Tqd is commonly intermingled with TKlg, mostly subparallel to the dominant foliation, but locally cuts across lithologic units (Figure 4i). Previous ages include ca. 40 Ma dates by U-Pb zircon ID-TIMS (Wright & Snoke, 1993) and SHRIMP (Premo et al., 2014), and we provide two new, but similar, U-Pb zircon ages in this study.

The Tmg unit is moderately to strongly foliated and lineated. It is an equigranular biotite monzogranite and lesser tonalite and granodiorite (Batum, 1999). Tmg is commonly exposed as tabular sheets (up to 70 m thick but typically 1–10 m) that are concordant to slightly discordant to foliated paragneiss. Existing ages for this unit are older U-Th-Pb zircon and monazite ages from Lamoille Canyon in the Ruby Mountains of 29 ± 0.5 Ma (Wright & Snoke, 1993). Two new ages are reported in this study.

All mylonitic bedrock units are cut by rare and poorly exposed subvertical, undeformed aphyric basaltic dikes. Dikes strike north and are up to 1 m wide. These were dated at ca. 17–15 Ma (Dee et al., 2015; Snoke, 1980; Zuza,

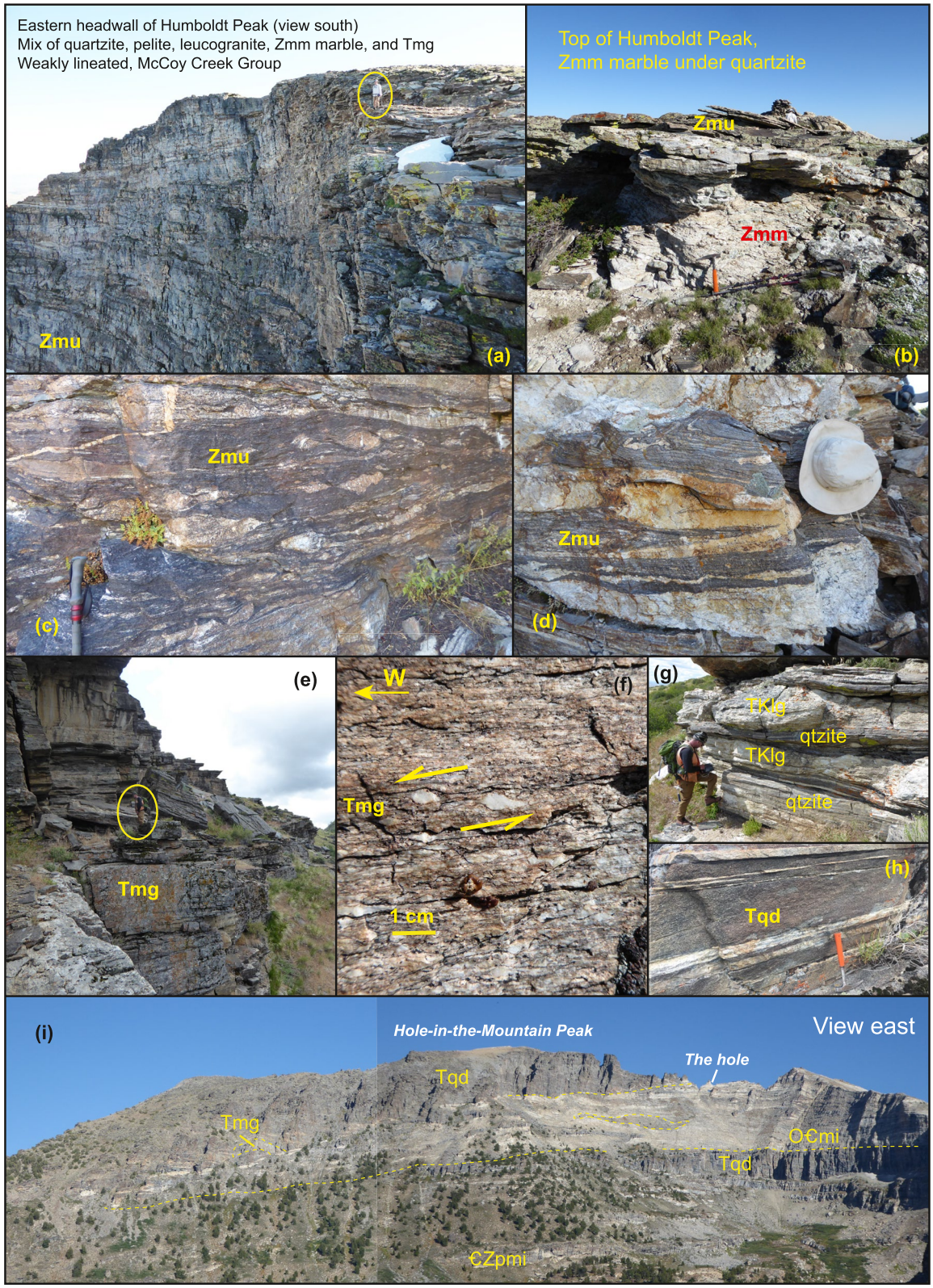
Eastern headwall of Humboldt Peak (view south)
Mix of quartzite, pelite, leucogranite, Zmm marble, and Tmg
Weakly lineated, McCoy Creek Group
Zmu
(a)
Top of Humboldt Peak,
Zmm marble under quartzite
Zmu
Zmm
(b)
Zmu
(c)
Zmu
(d)
(e)
Tmg
W
(f)
Tmg
1 cm
(g)
TKlg
qtzite
TKlg
qtzite
(h)
Tqd
(i)
Hole-in-the-Mountain Peak
View east
The hole
Tqd
Tmg
O€mi
Tqd
€Zpmi

Figure 4.

Henry, et al., 2021). In the southern Tent Mountain quadrangle in Dorsey Creek, a basalt dike cuts mylonitic fabrics and is truncated by brittle detachment faulting. This dike has a whole-rock $^{40}Ar/^{39}Ar$ date of ca. 16.8 Ma (Zuza, Dee, et al., 2021), thus indicating that all or some detachment slip occurred after ca. 16.8 Ma. Basalt dikes near Angel Lake have a ca. 17.3 Ma plagioclase $^{40}Ar/^{39}Ar$ age and basalt lava in the Clover Creek sequence, northeast of the East Humboldt Range, has a date of ca. 15.3 Ma (Zuza, Henry, et al., 2021; Figure 1c).

The west-northwest part of the map area consists of Miocene-Pliocene Humboldt Formation conglomerate, sandstone, shale, tephra, and tuffaceous sediments that may be underlain by Eocene Elko Formation. These deposits are bound on the west by the Quaternary active west-dipping Ruby Mountain frontal fault zone and on the east by a west-dipping, but less recently active normal fault against the bedrock (Figure 2). Age constraints for these sediments include detrital $^{40}Ar/^{39}Ar$ feldspars ages that require the sediments to be younger than 23 Ma, and ages from four tephra samples that range from 15.77 Ma to as young as 5.15 Ma (Zuza, Henry, et al., 2021). The Miocene sediments are interbedded with 15.3 Ma Jarbidge-type (Brueseke et al., 2014) rhyolite (Figure 2).

Quaternary (mid-Pleistocene to present) surficial deposits cover the western lower elevation regions, including a variety of alluvial fan surfaces, landslide deposits, glacial moraines, and glacial outwash deposits. There are at least two generations of glacial deposits. Cosmogenic ^{10}Be exposure dating constrain Qgo_1 to 13–27 ka and Qgo_2 to 120–130 ka (Figure 3a; Zuza, Dee, et al., 2021), which correspond with the ages of the Angel Lake and Lamoille glaciations, respectively (Laabs et al., 2013; Osborn & Bevis, 2001; Wesnousky et al., 2016).

3.3. Important Field Relationships

The following field relationships are shown in the geologic map (Figure 2) and the published 1:24,000-scale map (Zuza, Dee, et al., 2021). Here, we briefly summarize the field relationships most relevant to this study. The west side of the East Humboldt Range is bound by the Quaternary active, west-dipping Ruby Mountains frontal fault zone, which extends for more than 60 km to the southwest. In our study area, the fault steps west, resulting in a broad, hanging wall uplift underlain by the Miocene to Pliocene Humboldt Formation that dips gently north-northeast, although these dips are variable (Figure 2; Zuza, Dee, et al., 2021). The western range-bounding fault zone (Figure 2) had several late Quaternary surface-rupturing earthquakes that are recorded by increased uplift and dissection of Quaternary surfaces as a function of relative age (Wesnousky & Willoughby, 2003). Lidar elevation data shows fault scarps in glacial outwash surfaces, with average vertical separations of 5.2 m in Qgo_1 (younger) and 16.5 m in Qgo_2 (older). Using recent cosmogenic ^{10}Be exposure ages (Zuza, Dee, et al., 2021) this suggests that the western range-bounding normal fault (Figure 2) has an approximate vertical separation rate of ~0.21–0.35 mm yr^{-1} in the latest Pleistocene and a longer term late Pleistocene rate of ~0.09–0.17 mm yr^{-1}.

The Miocene-Pliocene Humboldt Formation is interbedded with Jarbidge-type rhyolite. The base of this section is not exposed, but its attitudes and map relationship suggest a thickness of at least ~3 km if there are not unrecognized faults duplicating the section (Dee et al., 2015; Zuza, Dee, et al., 2021). Projection of the ca. 15.3 Ma rhyolite exposures suggest ~1.25 km displacement on the bedrock-bounding, eastern range-bounding normal fault system (Figure 2c). Assuming faulting started after rhyolite deposition, this implies a post-15.3 Ma fault-slip rate of >0.08 mm yr^{-1} or a vertical separation rate of >0.05 mm yr^{-1} on the eastern range-bounding normal fault (Figure 2). Seismic reflection profiles suggest that the Humboldt Formation is >5 km thick on the westside of the Ruby Mountains and East Humboldt Range (e.g., Colgan et al., 2010; Satarugsa & Johnson, 2000). The seismic sections suggest growth strata and tilt fanning, which is not resolved in the field due to poor exposure. These observations are consistent with the inferred syn-extensional nature to these deposits (Colgan et al., 2010).

Most of the sub-detachment bedrock units are strongly foliated, lineated, and clearly mylonitized as evidenced by strong grainsize reduction and shear fabrics. Foliations parallel rock unit contacts, although original bedding is entirely transposed by mylonitic foliation. The dominant lineation trends ~280°–290° (Figure 2). The overall

Figure 4. Field photographs showing represented geologic units and structural relationships in the study area of the western East Humboldt Range. Photo locations in Figure 3 or listed here. (a) Humboldt Peak east-facing cirque and Zmu paragneiss (circled person for scale) with (b) interbedded Zmm marble with quartzite and pelite (location 40.903130, −115.119521). (c, d) Pelitic and migmatitic Zmu. (e) Tabular Tmg cliff (circled person for scale). (f) Top-west shear-sense observed in plagioclase porphyroclasts in Tmg. (g) Sill-like pods of TKlg with quartzite-dominated paragneiss, typical of paragneiss and igneous relationships. (h) Tqd appears less foliated and less lineated, but is still deformed and interlayered with TKlg and ЄZpmi quartzite (lowest gray horizon). (i) Photomosaic of Hole in the Mountain, showing the Tqd intruded OЄmi-ЄZpmi contact. (j) Tqd intruded Zmm marbles with rusty garnet-rich calc-silicate horizons near intrusive contacts. (k) Paragneiss host rock intruded by Tqd with wisps of TKlg (circled person for scale). (l) Fold within Zmm marble with hinge parallel to lineations observed in quartzite, interpreted as an *a*-type fold. (m) Boudinage of siliciclastic and leucogranite layers within OЄmi marble. (n) Common chaotic tight folding of siliciclastic horizons at the lowermost parts of the OЄmi unit.

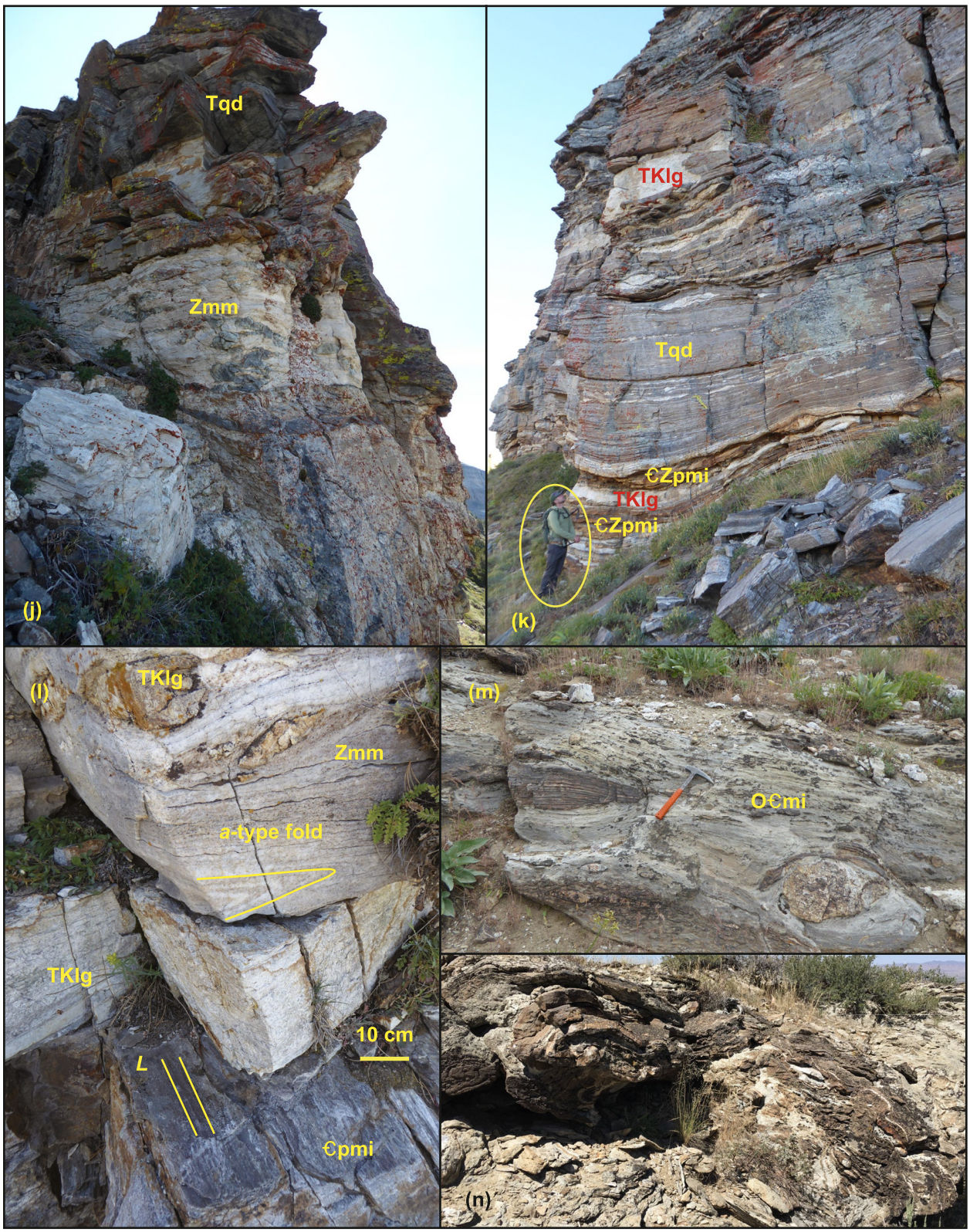

Figure 4. (Continued)

Figure 5. Field photographs of structurally higher mylonitic samples, including (a) Mississippian Diamond Peak Formation and (b) Ordovician Eureka Quartzite (Oe) with overlying Ordovician Fish Haven Dolomite (Ofh) and DOd. (c, d) Photos showing undeformed leucogranite (Tlg) cutting mylonitic fabrics. Photo locations: (a) 40.83177, −115.14803; (b) 40.941456, −115.22479; (c) 40.911154, −115.130304; and (d) 40.950277, −115.220804.

range structures consist of subhorizontal foliations toward the range crest and a gentle west dip toward the western range flank (see stereonet in Figure 2). Units are in largely in upright stratigraphic order, with Zmu and ЄZpmi at structurally deeper levels and OCmi to Oe structurally higher. Oe is observed over OCmi marbles in the western map area, but is also exposed in a drainage cliff as shown in Figure 5b. The DOd dolomites and marbles structurally and stratigraphically overlying Oe are the highest stratigraphic units in the lower plate (i.e., mylonitized and

sheared) observed in the study area. The rocks from ЄZpm to Oe have a structural thickness of ~700 m based on map projections and cross-sections (Figure 2b). We sampled the strongly mylonitized Mdp outcrops in the adjacent Secret Valley quadrangle (Snoke et al., 2021) to the southeast, which was thus the structurally highest part of the lower plate observed in this study.

In our mapping, we observed that the Msq unit was structurally below deformed Ordovician rocks (i.e., Oe and OЄm) and above ЄZpmi, which implies a complex structural history. One interpretation is that Ordovician (OЄm and Oe) rocks were thrust over Mississippian rocks (Msq) during the Mesozoic; similar stratigraphic separation is observed across the Independence thrust in the Pequop Mountains to the east (Zuza, Henry, et al., 2021; Figure 7). This sequence would have then been severely attenuated and thinned to ultimately place Msq over ЄZpmi. Alternatively, there may have been tight recumbent and overturned detachment folding that leads to the observed relationships. The recumbent folds in both the Ruby Mountains and East Humboldt Range could lead to complex overturned relationships with units variably missing from the structural section. Here, we tentatively interpret that this sequence resulted from Mesozoic thrust faulting followed by Cenozoic attenuation (Figure 7), but acknowledge this is a nonunique model to explain this complex structural relationship.

Almost all bedrock units in our map area (Figure 2) show top-west shear sense (Figure 4f) based on observed C-S fabrics in the deformed igneous rocks, mica fish, asymmetric porphyroclasts, and asymmetric folds. Rare small-scale folds all have fold hinges parallel to the dominant west-northwest-trending lineations (Figure 4l), which we interpret as local *a*-type folds (Hacker et al., 2000; Malavieille, 1987; Mattauer, 1975; Sander, 1930) or incompletely exposed sheath folds. Rare top-east shear fabrics or asymmetric folds were observed at deeper structural levels, and these may reflect an older shear fabric that was overprinted by Cenozoic top-west mylonitization (McGrew, 1992, 2018; McGrew & Casey, 1998).

Important crosscutting field relationships in the study area, from oldest to youngest, are as follows. (a) Poorly resolved Mesozoic deformation and possible unit duplication (?) (Figure 7) is variably overprinted by Cenozoic attenuation and mylonitization. (b) An older phase (or phases) of TKlg intruded the main bedrock units, presently exposed as foliation-parallel pods and sheets. This may be syn-kinematic with Mesozoic deformation and tectonic burial. (c) A large Tqd body intruded, focused along the ЄZpm-OЄm contact, especially by Hole-in-the-Mountain peak (Figure 4i). Tqd and TKlg are complexly intermingled (Figures 4h and 4k). (d) Tmg intruded all units as large tabular sheets, with sparse dike relationships. Structurally deeper levels have very large volumes of Tmg with steep ~10–40 m wide dikes (Figure 6). (e) The entire section was attenuated and sheared. MЄmu down to ЄZpmi is most strongly mylonitic, and at structurally deeper levels shear fabrics diminish. (f) Younger, sparsely observed leucogranite dikes cut mylonitic fabrics at shallow to steep dips (Figure 5d); leucogranite is also observed cutting Tmg at deeper structural levels (Figure 6). (g) Undeformed subvertical north-striking basalt dikes intrude the mylonitized rocks (Figure 2). (h) Detachment faulting places non-metamorphosed upper Paleozoic rocks over the mylonitic rocks and cuts the basalt dikes. (i) High-angle normal faulting exhumes the range, and Miocene sediments discussed above were deposited along the western flank of the range. Contemporaneous middle Miocene rhyolite lava flows and tephra were deposited.

Just north of the map area is the west-trending, recumbent, isoclinal northward opening Winchell Lake nappe (Henry et al., 2011; McGrew, 2018; McGrew et al., 2000), a fold that involves Mississippian rocks near its core and Neoproterozoic McCoy Creek Group rocks on its limbs (Figure 8). This fold is well exposed in high cirque walls in the central East Humboldt Range. The geometry of this fold relies on interpretations of its folded, and pervasively intruded, units, including ЄZpmi, OЄmi, Oe, Dod, and Mississippian clastic units. Here, we present carbon isotope and detrital zircon data to confirm these age relationships. Our mapping is consistent with the overall interpretations of McGrew (2018) that the recumbent syncline was juxtaposed by a fault against relatively coherent ЄZpm-OЄm stratigraphy. In our study area, apparently upright ЄZpm along the northernmost west-trending ridge in Figure 2, just north of Ackler Creek, trends into the Winchell Lake nappe to the east and is structurally above the main package of ЄZpm-OЄm stratigraphy that makes up most of the map area to the south. Relationships with the Winchell Lake nappe imply that the rocks on this ridge become overturned toward the northeast, but they are juxtaposed against upright ЄZpmi-OЄm in Ackler Creek (Figure 2). We inferred a queried thrust fault that links along strike to the east with a nappe-emplacement thrust interpreted by McGrew (2018), but poor exposure and similar hanging wall-footwall units makes this structure ambiguous. This nappe fold, and others to the south in the Ruby Mountains, may have formed in the Late Cretaceous (McGrew, 2018; McGrew et al., 2000), Cenozoic (MacCready et al., 1997), or during a complex polyphase history.

Figure 6. Field photographs of structurally deeper rocks near Steele Lake in the Humboldt Peak quadrangle of McGrew (2018). (a) Uninterpreted and interpreted photos across Steele Lake showing relationship between subvertical Tertiary monzogranite (Tmg) and Tertiary leucogranite (Tlg) dikes. Box shows approximate view in (b). (b) Close-up view of Tlg cutting across Oligocene Tmg, thus requiring Oligocene or younger age to some of the Tlg unit. (c) View of Tmg cutting foliated Zmu quartzite. Tmg is weakly foliated and lineated. Photo locations: (a, b) 40.915826, −115.113429; and (c) 40.914018, −115.109019.

4. Analytical Methods and Results

4.1. U-Pb Zircon Geochronology Methods

Igneous zircon U-Pb dating was conducted to constrain the ages of mylonitized intrusions Tqd and Tmg. Detrital zircon U-Pb dating was conducted to better constrain the age of important sedimentary rocks in the study area, including mapped Oe and Mdp/Msq units. Detrital zircon ages of these rocks were compared against better constrained rock units from elsewhere in the eastern Great Basin. First, we analyzed a known Oe sample from the Pequop Mountains (sample PFW1; Figure 1), which was compared with three probable Oe samples from the East Humboldt Range in and around the Winchell Lake nappe. Additionally, the interpretation of strongly attenuated Mdp/Msq was tested via detrital zircon comparison. Separation and analytical details are in the Supporting Information.

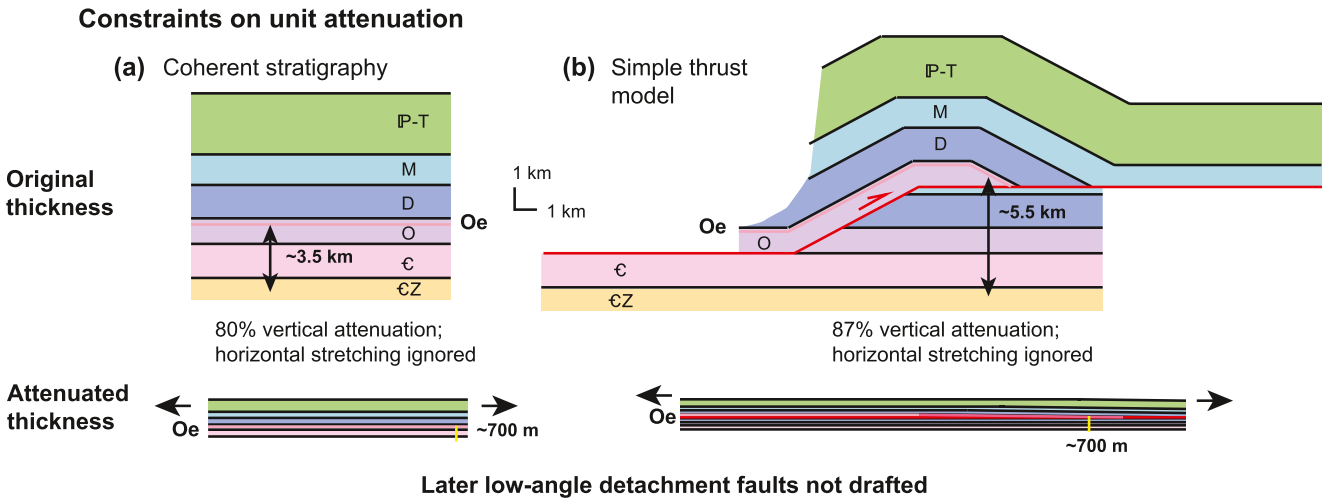

Figure 7. (a) Sketch of possible attenuation of the coherent Oe to €Z footwall stratigraphy from ~3.5 km to 700 m. (b) A model to explain the thrust relationships in Figure 2 as a simple pre-Cenozoic thrust fault that places Ordovician marbles onto Mississippian siliciclastic rocks. Attenuation of this relationship would result in a similar map pattern as observed in the southwest corner of Figure 2.

Detrital zircon results were compared against known Oe data from PFW1 (this study) and a compilation of Oe and Neoproterozoic strata ages (Gehrels & Pecha, 2014). Data were plotted as normalized probability density plots, compared qualitatively, and statically evaluated via DZstats v2.3 (Saylor & Sundell, 2016) with a Kolmogorov-Smirnov (K-S) test and multi-dimensional scaling (MDS; Vermeesch, 2013). The K-S test explores the likelihood two compared samples are from the same parent population, and when the p value is <0.05, there is a 95% that two compared samples are from dissimilar populations. With MDS, samples are visually mapped to explore their similarity by minimizing misfit ("stress") between disparities, which results in similar samples concentrating together whereas dissimilar samples are farther apart.

4.2. Zircon U-Pb Geochronology Results

Four igneous and 6 detrital zircon samples were analyzed for zircon U-Pb dating. Complete data tables and concordia plots for zircon analyses are in the Supporting Information, including Supporting Table S1. Summary

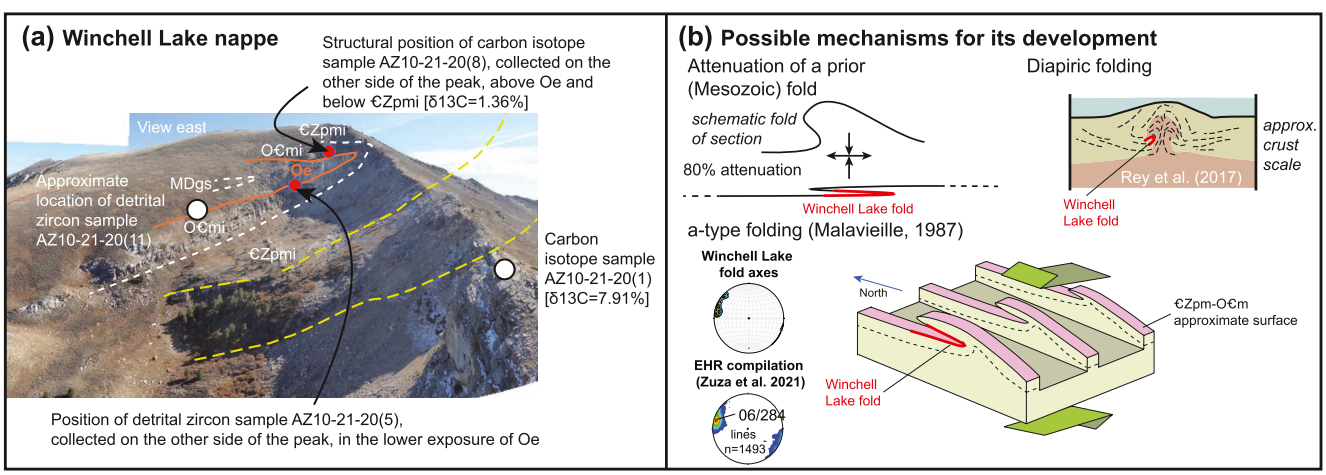

Figure 8. (a) Annotated photomosaic of the Winchell Lake fold nappe in the East Humboldt Range, showing approximate stratigraphic contacts and positions of collected detrital zircon and carbon isotope samples. These analyses confirm drafted age assignments. (b) Possible models for the generation of the isoclinal, recumbent fold: a prior generation of folding could have been strongly attenuated, recumbent overturned folds could have been generated during diapiric metamorphic core complex upwelling, or the fold could have developed during top-west mylonitic shearing as an *a*-type fold (note parallel fold hinge and stretching lineations; after Malavieille, 1987). See text for discussion.

Table 1
Zircon U-Pb Summary Age Table

Sample	Latitude	Longitude	Map unit	Lab	Mean age (Ma)	MSWD	n^a
Igneous analyses							
AZ8-19-19(6)	40.95752	−115.20163	Tmg	1	31.3 ± 0.2	1.1	21/25
AZ7-28-20(4)	40.990739	−115.12566	Tmg	3	32.5 ± 0.3	1.6	29/40
060720-4	40.950218	−115.22081	Tqd	2	39.9 ± 0.2	1.9	67/109
AZ 6-30-20 (6)	40.954877	−115.22200	Tqd	3	38.7 ± 0.3	1.6	34/41
Detrital analyses							
AZ 10-20-20 (1)	40.941456	−115.22479	Msq	1	-	-	-
HR 12-03	41.025861	−115.09167	Oe	1	-	-	-
AZ 10-21-20 (5)	40.98838	−115.105	Oe	1	-	-	-
AZ 10-21-20(11)	40.99079	−115.112	Oe	1	-	-	-
AZ 10-8-19(1a)	40.83177	−115.14803	Mdp	1	-	-	-
PFW1	40.97812	−114.5700	Oe	3	-	-	-

Note. Laboratories: (1) Arizona LaserChron; (2) UC Santa Barbara; and (3) University of Nevada, Reno.
[a]n = number of analyses in mean over the total number of analyses or grains analyzed for detrital.

ages and sample locations are in Table 1. Monzogranite sample AZ8-19-19(6) was collected from a large tabular monzogranite body on the western flank of the map area. Twenty-five zircons were analyzed. All analyses were concordant with ages spanning ca. 35–31 Ma. The weighted mean age of the dominant population of 21 grains was 31.3 ± 0.2 Ma (MSWD: 1.1), which we interpret as the crystallization age of this sample.

Sample AZ7-28-20 (4) was collected from a monzogranite ridge-forming exposure in the northeast corner of the map area. Of 40 zircons analyzed, 31 were concordant, spanning ca. 29 Ma to ca. 83 Ma. Excluding the single youngest age that lies outside the dominant ca. 32 Ma population and the older Cretaceous age yields a weighted mean age from 29 analyses of 32.5 ± 0.3 Ma (MSWD: 1.6). This is interpreted as the crystallization age of the sample.

Both analyzed quartz diorite samples yielded a significant population of inherited zircons. Quartz diorite sample 060720-4 was collected from a ~5 m thick sill. Analysis of 109 grains yielded diverse ages including several 2.5 Ga ages, some Mesoproterozoic ages, a few Cretaceous grains, and mostly Eocene dates. The weighted mean age of the dominant population of concordant Eocene grains (n = 67) was 39.9 ± 0.2 Ma (MSWD: 1.9), which we interpret as the crystallization age of this sample. The older zircon grains were inherited.

Forty-one grains were analyzed from quartz diorite sample AZ 6-30-20 (6), collected from Tqd sills that intruded O€mi marbles along the west fork of Boulder Creek. Analyses yielded a dominant Eocene population and several grains >2.0 Ga. The weighted mean age of the dominant concordant youngest population of analyses (n = 34) yielded a weighted mean age of 38.7 ± 0.3 Ma (MSWD: 1.6). In summary, the new zircon U-Pb igneous ages confirmed an Eocene age, ca. 38–40 Ma, for the quartz diorite unit and Oligocene age, 31–33 Ma, for the monzogranite unit in the East Humboldt Range, consistent with previous ages (Premo et al., 2014; Wright & Snoke, 1993).

To serve as a reference of detrital zircon spectra, PFW1 was collected from well-constrained Oe quartzite exposures in the Pequop Mountains (Table 2; Figure 1). Of 139 analyses, 138 were concordant, with ages spanning ca. 1.0 Ga to ca. 3.0 Ga (Figure 11). This Oe sample displayed a prominent ca. 1.85 Ga age population, with lesser Paleoproterozoic ages.

Detrital zircon samples AZ 10-21-20 (11) and AZ 10-21-20 (5) were collected from probable Oe quartzite from the lower upright limb of the Winchell Lake nappe, just northeast of the study area (McGrew, 2018; Figure 8). Sample AZ 10-21-20 (11) yielded a range of Late Cretaceous to 3.0 Ga ages, with many discordant analyses. Most Late Cretaceous ages were discordant, had Th/U ratios <0.1, and defined a discordia line with Late Cretaceous lower intercept, and thus these analyses were interpreted as metamorphic zircons or overgrowths

Table 2
Samples for Microstructural Observations and Electron Backscatter Diffraction Analyses

					Vollmer (1990) ternary						
Sample	Unit	Step (μm)	*M*	*K*	*P*	*G*	*R*	Recrystallized grainsize (μm)[a]	Flow stress (MPa)	Latitude	Longitude
AZ10-8-19 (1a)	Mdp	2.5	0.02	0.95	0.10	0.16	0.73	-	-	40.83177	−115.14803
"	"	0.2	-	-	0.14	0.16	0.71	3.41 ± 1.11	209	"	"
AZ 7-1-20 (1)	Oe	1	0.09	0.88	0.26	0.30	0.45	6 ± 2.3	146	40.936922	−115.23821
AZ 10-20-20(1)	Msq	5	0.11	0.24	0.21	0.50	0.29	-	-	40.941456	−115.22479
"	"	1	0.24	0.57	0.47	0.37	0.16	6.6 ± 3.2	138	"	"
AZ 7-2-20(4)	Zmu	5	0.39	0.28	0.67	0.30	0.03	83.8 ± 51.9	28	40.946568	−115.15773
AZ 6-30-20 (2)	ЄZpmi	3	0.34	0.10	0.60	0.38	0.02	37.4 ± 21.3	46	40.949227	−115.21765
AZ8-19-19-(2)	Tmg	5	0.24	2.66	0.53	0.19	0.28	21.9 ± 10.2	65	40.95774	−115.1994
AZ8-19-19-(4)	ЄZpmi	5	0.39	0.82	0.68	0.25	0.07	35.4 ± 20	48	40.95701	−115.17796
AZ8-19-19-(5)	ЄZpmi	5	0.49	1.51	0.79	0.16	0.04	50 ± 28.9	39	40.95703	−115.17836
020,619_5	ЄZpmi	5	0.28	0.35	0.51	0.39	0.09	37.8 ± 22.9	46	40.86400	−115.24400
AZ 8-4-18 (3)	ЄZpmi	5	0.37	0.90	0.66	0.26	0.08	57.7 ± 35.9	35	40.841632	−115.13982
"	"	2	-	-	0.72	0.24	0.03	37.5 ± 25.9	46	"	"
AZ8-4-18 (1)	ЄZpmi	5	0.38	0.09	0.61	0.30	0.09	-	-	40.841583	−115.13997
"	"	2	-	-	0.54	0.37	0.09	33.5 ± 19.9	50	"	"

[a]Calculated using Cross et al. (2017) MTEX code.

(Figure S2 in Supporting Information S1). The remaining population of concordant ages (n = 29) spanned Proterozoic-Mesoarchean with a prominent ca. 1.85 Ga age population (Figure 11). Sample AZ 10-21-20 (5) yielded mostly concordant ages and 182 concordant grains yielded a range of Proterozoic-Mesoarchean ages, with a prominent ca. 1.8–1.85 Ga peak. Sample RH 12-03 was collected from Angel Lake from mapped Oe (McGrew & Snoke, 2015; Figure 1). A total of 177 grains were analyzed, and except for a single younger grain (i.e., Phanerozoic) and discordant analyses, most ages were Paleoproterozoic and Archean with a prominent ca. 1.8–1.85 Ga peak (Figure 11).

The Msq quartzite sample AZ 10-20-20 (1) was collected from a large Msq exposure in the southwest corner of the map (Figure 2). A total of 224 grains were analyzed, and 200 concordant analyses spanned ca. 299 Ma to 2.85 Ga. The Mdp sample AZ 10-8-19(1a) was collected from the Secret Valley quadrangle (Snoke et al., 2021; Figure 1). Only 92 grains were analyzed, and 84 concordant analyses spanned ca. 382 Ma to ca. 3.0 Ga. Both Msq and Mdp samples yielded a ca. 1.8 Ga age peak, a minor ca. 2.6 Ma population, and a subdued range of ca. 1.5–1.7 Ga ages (Figure 11).

All samples were compared against compilation spectra from Gehrels and Pecha (2014) for Oe and Neoproterozoic rocks from Utah and Nevada (Figure 11). Qualitatively, Oe spectra analyzed in this study resemble the Gehrels and Pecha (2014) data set, with the Msq and Mdp samples appearing most dissimilar due to the ca. 2.6 and 1.5–1.6 Ga age populations. The K-S test (inset of Figure 11a) shows that Oe samples were broadly similar to each other, and the Mdp/Msq samples were dissimilar to all but one Oe sample (95% with $p < 0.05$ in all comparisons). As expected, the Neoproterozoic compilation of Gehrels and Pecha (2014) was dissimilar from all Oe and Mdp/Msq analyses (Figure 11a). In the MDS comparison, all Oe samples cluster together, the Mdp and Msq samples were similar but distinctly different from Oe, and the Neoproterozoic analyses from Gehrels and Pecha (2014) were most dissimilar. These detrital zircon comparisons suggest that all of the strongly mylonitized analyzed Oe in the East Humboldt Range had similar detrital zircon spectra to other known Oe exposures in the Pequop Mountains and broader Great Basin, which confirms previous age assignments. The Mdp and Msq samples were subtly distinct from Oe. However, Mississippian strata do not have unique detrital zircon records, due in part because they were deposited as recycled detritus from an eroded Antler highland to the west (e.g., Beranek et al., 2016; Poole & Sandburg, 1977; Speed & Sleep, 1982). That said, these samples were dissimilar to Oe and Neoproterozoic rocks. The limited abundance of siliciclastic rocks in the Neoproterozoic-Paleozoic

section supports the Mississippian age call. There are several thin quartzite or quartz arenite units in the Cambrian through Devonian stratigraphy (e.g., Cambrian Morgan Pass, Shafter, or Dunderberg Formations, Ordovician Kanosh quartzite, or in the Devonian Guilmette; Zuza, Henry, et al., 2021), and it remains possible that this exposure is older than its Mississippian assignment.

4.3. Whole-Rock Igneous Geochemistry Methods

To characterize igneous rocks in the study area, and understand their petrogenesis, we conducted whole-rock geochemical analyses on representative samples. Samples were collected, cleaned, and crushed, using 10–50 grams per analysis. Analyses were conducted by ALS Geochemistry in Reno, Nevada. Major element analyses were completed by fused bead and acid digestion preparation and analyzed using an inductively coupled plasma atomic emission spectroscopy. Rare and trace element analyses were also completed by fused bead and acid digestion preparation and analyzed using an inductively coupled plasma mass spectrometer. For classification and discrimination diagrams, major oxides were normalized to anhydrous values.

4.4. Whole-Rock Geochemistry Results

Geochemical data is provided in Table S3 in Supporting Information S1. Silica content for each of the main deformed igneous units show discrete clusters, with the Eocene quartz diorite units being most mafic (~65–70 SiO_2 wt%), the Oligocene monzogranite being fairly felsic (>70–75 SiO_2 wt%), and the analyzed Cretaceous-Tertiary leucogranites overlapping the monzogranite but in general being most felsic (>75 SiO_2 wt%). The two analyzed basalt dikes were noticeably more mafic (<60 SiO_2 wt%), with sample AZ 6-30-20(1) showing anomalously high Nb and Ta.

4.5. Carbon Isotopic Analyses Methods

Carbon isotopic analyses were conducted to investigate differences between Neoproterozoic and Paleozoic marbles, as suggested by Wickham and Peters (1993). Specifically, earlier mapping interpreted that most marbles were part of the O€m unit (Hurlow, 1987), but more recently it has been appreciated that Neoproterozoic marbles exist within the €Zpmi/Zmu unit (e.g., McGrew, 2018). Hurlow (1987) interpreted that some of the marbles found interlayered with siliciclastic paragneiss were complexly infolded and interwoven O€mi marbles, dragged to stratigraphically and structurally deeper levels.

Bulk carbonate samples were analyzed for the $^{13}C/^{12}C$ content at the Beijing Createch Testing Technology Company using a MAT253 with a GasBench II peripheral device. The results are expressed in delta (δ) notation relative to the V-PDB standard. Repeated analyses of laboratory standard carbonates (TTB1) with known $\delta^{13}C$ values were performed daily to ensure instrumental accuracy. The analytical errors of the laboratory standard were better than $\pm 0.1‰$.

4.6. Carbon Isotopes Results

Thirteen samples were collected for carbon isotopic analyses, including 12 from the East Humboldt Range study area and one from the Pilot Range. In the East Humboldt Range, three samples were collected from mapped Zmm marbles, whereas nine were collected from probable O€mi marbles. A few O€mi samples were from ambiguous structural positions, with substantial Quaternary cover surrounding them, and thus their analyses were conducted as tests of their unit call. The single Pilot Range sample was collected from a thick sequence of McCoy Creek Group strata (D. M. Miller, 1984), and thus this sample was an external test of the carbon isotope results.

Sample location information and isotopic results are in Table S4 in Supporting Information S1. Analyses yielded a bimodal distribution of $\delta^{13}C$ values: four samples had $\delta^{13}C$ values between 6.62 and 10.23‰, whereas eight samples had $\delta^{13}C$ values of <2‰ (mostly negative; Figure 12). The extremely positive $\delta^{13}C$ values were from Neoproterozoic marble samples and the negative $\delta^{13}C$ values were from Cambrian-Ordovician marble samples. The Pilot Range sample was unambiguously from McCoy Creek Group marbles, and yielded $\delta^{13}C$ of 9.47‰. To compare with our results, probability distribution functions of analyses from Lizzie's Basin (Neoproterozoic McCoy Creek marbles; Wickham & Peters, 1992) and Secret Creek Gorge (Cambrian-Ordovician marbles;

Fricke et al., 1992) were plotted next to the new analyses (Figure 12). Consistent, very positive $\delta^{13}C$ values for Neoproterozoic marbles and negative (or close to 0‰) $\delta^{13}C$ values for the Cambrian-Ordovician marbles match the observations of Wickham and Peters (1993).

4.7. Microstructure and EBSD Methods

Oriented samples were collected from representative rock units across the East Humboldt Range. Thin sections were cut parallel to lineation and perpendicular to foliation, and microprobe polished. Microstructures and kinematics were observed via petrographic microscope (Figure 9). Samples were polished for ~8 hr on a vibrational polisher with 0.02 μm colloidal silica suspension to remove near-surface crystal lattice damage and to allow for EBSD analyses at the University of Nevada, Reno following methods outlined in Zuza et al. (2019). The EBSD analyses used a Nordlys Nano high-resolution detector and Oxford Instruments Aztec 3.3 acquisition software package on a JEOL 7100 FE-SEM housed in the Mackay Microbeam Laboratory. Individual run conditions are listed in Table S4 in Supporting Information S1, and post-processing was completed in AZtecHKL software and MTEX v. 5.1.1 (Bachmann et al., 2011). Pole figure plots were plotted on lower hemisphere stereonets, in sample reference frame, shown as scatter plots of all grains (Figure 10). Some samples were presented as orientation distribution functions (Ismaïl & Mainprice, 1998; Wenk & Wilde, 1972) of one-point-per grain analyses when the scatter plots were very diffuse. More plots are in Figure S5 in Supporting Information S1. Quartz misorientation axes with angles between 2° and 10° were plotted and contoured on inverse pole figures with 10° half width, using the approach of Piette-Lauzière et al. (2020) for recrystallized and relict grains (Cross et al., 2017). Interpretation of the misorientation axes in terms of active slip systems was guided by Neumann (2000).

In addition to pole-figure plots and analyses, the EBSD data was used to determine crystallographic preferred orientation (CPO) strength and shape, recrystallized grainsize, misorientation axes, and kinematic vorticity. CPO strength parameters were derived in MTEX, including K and M (Mainprice et al., 2015), and Vollmer (1990)'s point (P), girdle (G), and random (R) indices. Grain-size determinations were made using the methodology of Cross et al. (2017), which determined recrystallized vs. relict grains depending on the range intragranular of misorientations. The step size of analyses was always <20% the minimum average grainsize, which provided confidence in this approach.

4.8. Microstructure and EBSD Results

Eleven samples were collected from across the western and southern East Humboldt Range (Figure 1b and Table 2). All samples were quartzite, except Tmg sample AZ8-19-19-(2). In addition to quartz, lesser phases included mica and feldspar (Figure 9). Mica fish, C-S fabrics, and asymmetric porphyroclasts all suggest top-west shear sense (Figure 9). Example top-west indicators include S-C' relationships in Mdp sample (Figure 9a), tails on feldspar (Figure 9f), and mica fish (e.g., Figures 9e, 9g, 9h, 9j). Most samples were collected from a west-east traverse across the Tent Mountain quadrangle. An Oe sample AZ7-1-20 (1) was the structurally highest sample from this traverse (Figure 5b), collected from just outside of the southwest corner of the map in Figure 2. The structurally lowest sample, Zmu AZ7-2-20 (4), was collected from deep in a valley in the center of the range. To explore variations along strike, three samples were collected from Secret Valley to the south: Mdp samples AZ10-8-19(1a) and two ЄZpmi samples. Almost all samples revealed similar quartz microstructure and grainsize, with the exception of the structurally highest Oe and Mdp samples. Therefore, our microstructural observations are divided between (a) the majority of ЄZpmi-Zmu samples and (b) the structurally higher Mdp, Msq, and Oe samples.

For the ЄZpmi-Zmu samples, quartz grains show interlobate grain boundaries with minor polygonal textures (Figure 9). These textures are indicative of grain boundary migration recrystallization (GBM) and lesser subgrain rotation recrystallization (SGR; Hirth & Tullis, 1992; Stipp et al., 2002). Feldspar is dynamically recrystallized, forming tails on relatively larger porphyroclasts showing top-west shear sense (Figure 9f). The deepest Zmu sample is coarser grained and shows a clear GBM texture with interlobate grain boundaries (Figure 9k). The structurally higher samples showed distinctly different microstructures. Both Mdp and Msq samples display S-C' fabrics consistent with top-west shear (Figures 9a and 9c). The Msq sample was rich in organic carbon, and quartz grains possess polygonal textures of minor SGR and a core-mantle structure with very fine recrystallized bulging grain boundaries indicative of bulging recrystallization (BLG; Figure 9c; e.g., Stipp et al., 2002). Quartz grains

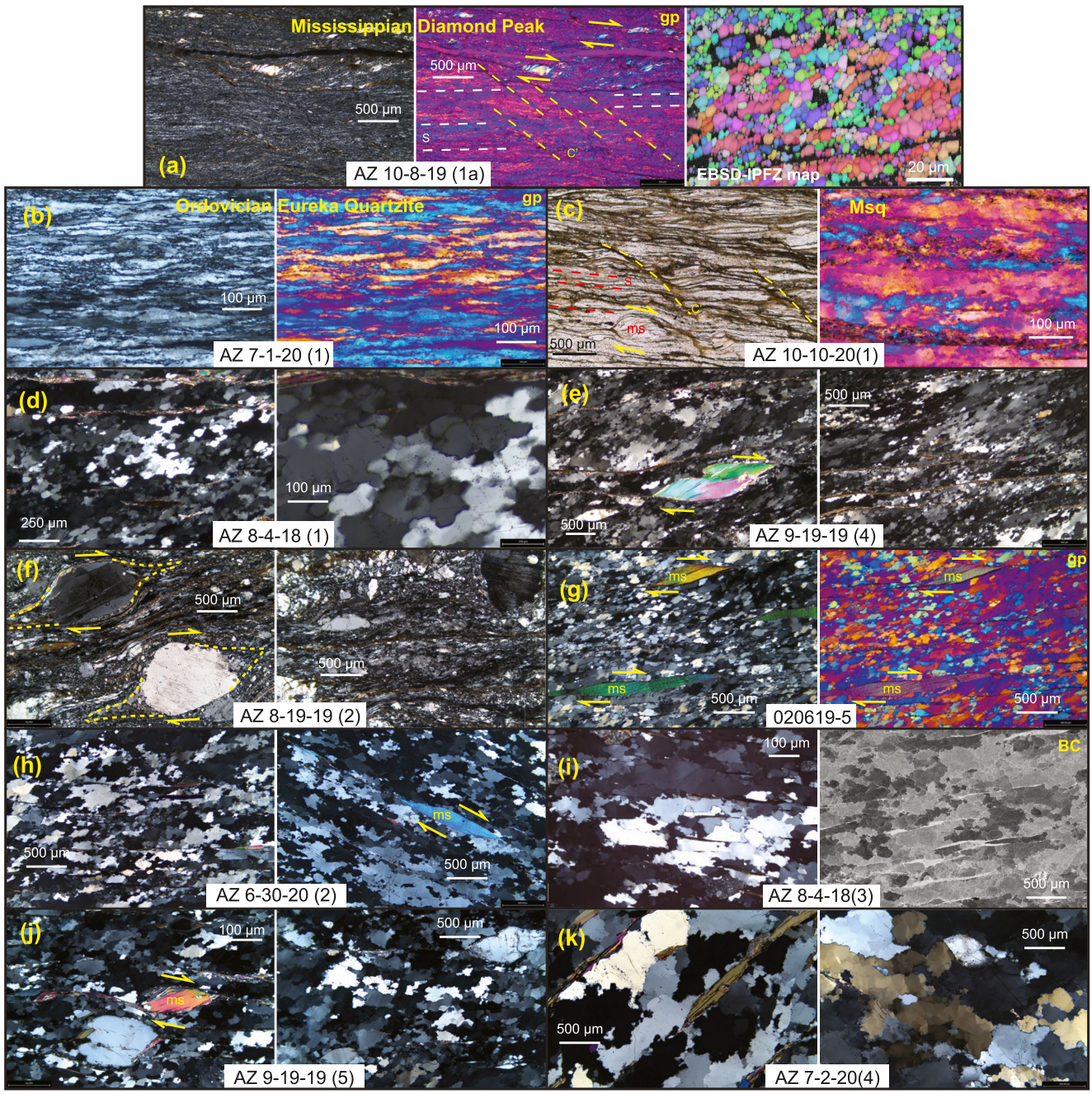

Figure 9. Photomicrographs of quartz-rich mylonite samples, revealing textures of dynamic quartz recrystallization. All samples are oriented so the right is west although foliation may not be horizontal in each photo due to stage rotation. Note all samples show clear top-west shear-sense indicators. Panel labeled GP has gypsum plate in and BC is a band-contrast map from EBSD analyses to show overall texture. Sample AZ10-8-19 (1a) shows an IPF-Z map to show finely recrystallized grainsize and evidence for possible diffusion creep deformation, including straight grain boundaries and four-way grain intersections. Samples are generally arranged so that the structurally higher samples are at the top and structurally deeper samples are at the bottom. Sample locations in Figure 1 and Table 2.

in the Oe sample were flattened, displaying a core-mantle BLG texture (Figure 9b). Sample Mdp is very finely recrystallized and comprised of almost entirely recrystallized grains (Figure 9a).

Quartz EBSD results (summarized in Table 2) show generally similar CPO patterns. Samples broadly show *c*-axis maxima normal to the thin sections (normal to the *xy* plane), parallel to fabric *z*-axis, in the center of the stereonets (Figure 10). Most *c*-axes show either short girdles or weak cross girdle geometries (Figure 10). For many of the samples, the girdles are roughly symmetric across the center of the pole figures, but some samples

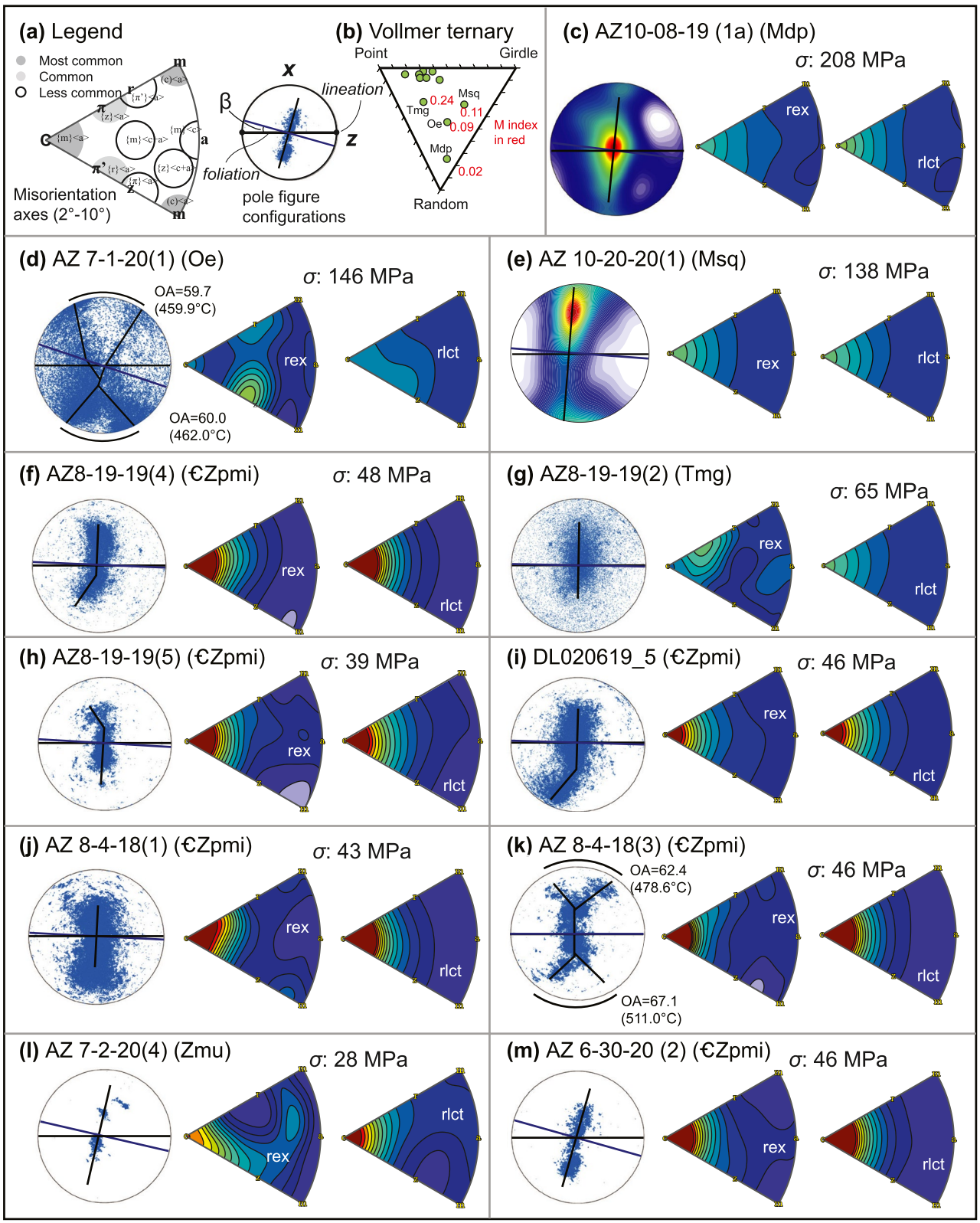

Figure 10. Quartz electron backscatter diffraction results for mylonite samples (additional plots in Figure S5 in Supporting Information S1). Samples are oriented so the right is west. (a) Legend for interpreting pole figure plots and misorientation inverse pole figures (IPF) plots derived from Neumann (2000). (b) Ternary of point, girdle, and random factors based on Vollmer (1990). (c–m) For each sample, a scatter plot of all analyses is shown for quartz *c* axes, except panels (c and e) where an orientation distribution function of one-point-per-grain is plotted due to more diffuse scatter. The right side of each panel are IPF of 2°–10° misorientation axes for relict (rlct) and recrystallized (rex) quartz grains (determined via Cross et al., 2017 script).

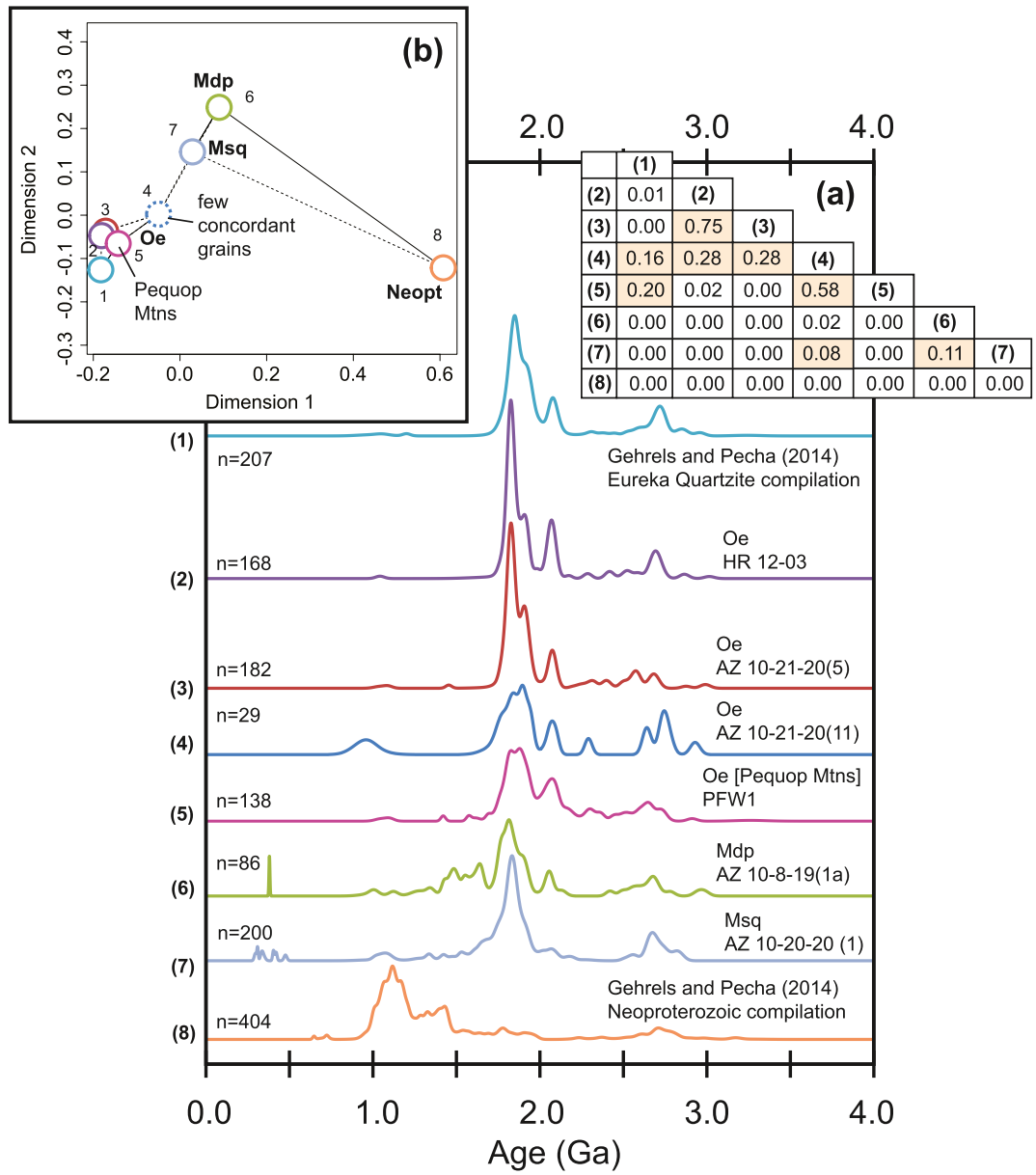

Figure 11. Detrital zircon results from this study on Ordovician Eureka Quartzite (Oe) and Mississippian clastic (Mdp and Msq) rocks. (a) Normalized probability plots of four new Oe analyses, one new Mdp analysis, and Gehrels and Pecha (2014) Oe compilation. Inset shows comparison results of K-S (Kolmogorov-Smirnov) test as p values, where values <0.05. (b) Multi-dimensional scaling plot showing how Oe samples are most similar, and the Mdp sample is distinct (e.g., Vermeesch, 2013).

show slightly top-right inclination of the girdles that is consistent with top-west shear sense (Figure 10). Crystallographic vorticity axis (Michels et al., 2015) analyses show that shear zone flow was plane-strain monoclinic (see Supporting Information), which allows interpretation of the CPO patterns with respect to possible active slip systems. The overall concentration of *c* axes near the center of the stereonet is consistent with predominately prism <a> slip, with lesser rhomb <a> to basal <a> activity in quartz (Barth et al., 2010; Toy et al., 2008). The dominance of prism <a> activity (Figure 10) is consistent with GBM (lesser SGR) recrystallization textures (Figure 9).

Fabric strength and shape were tracked via *K*, *M* indices, and *P*, *G*, and *R* terms (Table 2; Mainprice et al., 2004; Skemer et al., 2005). Most samples yielded *M* values between 0.2 and 0.5, indicating fairly strong fabrics strength.

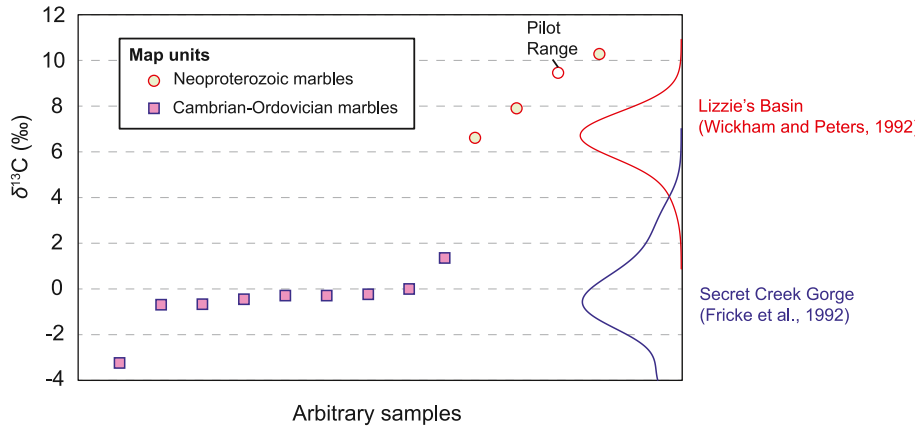

Figure 12. Carbon isotope data from the East Humboldt Range (one sample from the Pilot Range) showing distinct difference of $\delta^{13}C$ values for Cambrian-Ordovician marbles (low or negative values) and Neoproterozoic marbles (very positive values), with probability density plots of published data for Cambrian-Ordovician marbles (blue curve) and Neoproterozoic marbles (red curves). Analytical uncertainties are <0.06‰, which is smaller than the symbol size.

The outlier samples were the structurally higher samples AZ10-8-19 (1a), AZ 7-1-20 (1), and AZ 10-20-20 (1) that yielded *M* indices of 0.02, 0.09, and 0.11 respectively. These values are consistent with the relatively diffuse pole figure plots (Figure 10). Values of *K*, which reflects the shape distribution of the crystallographic axes, spanned ~0.09–2.6 with an average of 0.9. When $K = 1$, the crystallographic axes are at the transition between cluster distributions (Woodcock, 1977). Results for Vollmer (1990)'s *P*, *G*, and *R* terms were plotted on a ternary diagram (Figure 10b), which shows that most samples trended toward the point values (generally $P > 0.5$). The three prominent exceptions are Tmg sample AZ8-19-19-(2) and the structurally higher Oe and Mdp samples (Figure 10). We interpret that polyphase deformation (i.e., quartz and feldspar) or grain pinning in the Tmg sample may have disrupted its quartz CPO strength and its *M* index (0.24) is higher than the Oe and Mdp samples. The Oe sample plotted in the middle of the ternary diagram, conveying equal girdle, point, and randomness for its CPO fabric (Figure 10b). The Mdp sample (AZ10-08-19 (1a)) trended toward a random fabric, which is consistent with its pole figure dispersion (Figure 10).

For the low-angle (2°–10°) misorientation plots, almost all samples show maxima clusters near the *c*-axis for both recrystallized and relict grains, which is consistent with prism<a> slip (Neumann, 2000; Figure 10a). The structurally deepest sample, Zmu sample AZ 7-2-20 (4), showed some scatter in the misorientation plots toward the {z}<a + c> domain, possibly indicating minor {z} slip (Figure 10l). Two samples deviated from this trend: Tmg sample AZ8-19-19-(2) and Oe sample AZ 7-1-20(1). Recrystallized grains from the Tmg sample weakly cluster on the outer edge of the misorientation, suggesting rhomb<a> activity, whereas the relict grains concentrate near the *c* axis associated with prism<a> slip (Neumann, 2000; Figure 10g). Recrystallized grains from the Oe sample concentrate on the lower outer edge of the IPF plot, suggesting rhomb<a> activity, whereas the relict grains concentrate near the *c* axis and lower outer edge, associated with distributed rhomb and prism <a> slip (Neumann, 2000; Figure 10d).

Recrystallized grainsize was determined from the EBSD data (Cross et al., 2017). For the finest grained samples, additional maps were constructed using smaller stepsizes, and grainsize estimates were made using the finest stepsize maps. Results are summarized in Table 2. There is an overall trend of finer recrystallized grainsize with higher structural position, with Zmu sample AZ 7-2-20(4) yielding recrystallized grainsizes of ~84 μm and Mdp sample AZ10-8-19 (1a) yielding recrystallized grainsizes of ~3 μm. These grainsizes were translated to differential stresses using the sliding resolution piezometer of Cross et al. (2017), yielding stress estimates from 28 to 209 MPa for the range of observed recrystallized grainsizes (Table 2).

5. Discussion

5.1. Deformation Conditions

The East Humboldt Range mylonitic shear zone exhibits consistent top-west shear kinematics across its map- and cross-section distribution. The structurally highest samples displayed BLG quartz recrystallization, the structurally lowest samples showed GBM conditions, and many samples in between showed mixed GBM/SGR quartz recrystallization (Figure 9). The pronounced variation in recrystallization mechanism is most dominantly affected by temperature, although grain pinning, water content, and strain rate can also influence these shifts (e.g., Law, 2014; Lloyd & Freeman, 1994; Mainprice et al., 1986; Stipp et al., 2002). That said, we can qualitatively infer that the deepest GBM samples deformed at temperatures ~500–600+°C for GBM recrystallization mechanism, mixed SGR/GBM recrystallization probably operated at temperatures of ~500°C, and the structurally higher samples displaying BLG recrystallization may have deformed at temperatures ≤400°C (e.g., Blumenfeld et al., 1986, 1988; Hirth & Tullis, 1992; Jessell, 1987; Law, 2014; Lloyd & Freeman, 1994; Mainprice et al., 1986; Stipp et al., 2002). Dynamic recrystallization of feldspar grains (Figure 9f) supports deformation temperatures above ~450°C (e.g., Tullis & Yund, 1985).

The CPOs revealed by EBSD analyses show similar strength (M ~ 0.3–0.5, R < 0.1) for all analyses except for the mylonitized granite and the structurally highest samples (Table 2; Figure 10b). Most samples revealed predominately prism <a> slip in quartz, with lesser rhomb <a> activity (Figure 10). These slip systems are active at ~450°C–550°C (e.g., Barth et al., 2010; Okudaira et al., 1995; Stipp et al., 2002; Toy et al., 2008). These temperature estimates are similar to the above constraints from observations of dynamic quartz recrystallization. A few samples showed cross-girdle geometries, which were fit by hand for opening-angle thermometry (e.g., Law, 2014), using the calibration of Faleiros et al. (2016) with an uncertainty of ±50°C. This approach yielded temperature estimates of ~460°C for Oe sample AZ7-1-20(1) and ~500°C for ЄZpmi sample AZ8-4-18(3) (Figure 10).

The Mdp sample was the finest grained sampled (Figure 9a). EBSD data were consistent with predominately prism <a> and rhomb <a> slip activity (Figure 10c). However, this sample also displayed the weakest CPO (M: 0.02, R: 0.73; Figure 10b). To explain this, we suggest that this sample may display evidence for diffusion creep, including its very fine grainsize (~3 μm), straight grain boundaries, and four-way grain junctions (see IPFZ EBSD map in Figure 9a). Diffusion creep can potentially weaken CPOs (Bestmann & Prior, 2003; Jiang et al., 2000; Wightman et al., 2006). In this interpretation, dislocation creep would have generated finer grainsizes, associated with a stronger CPO, and the activation of diffusion creep may have weakened the CPO during grain-boundary sliding.

In summary, the quartz microstructure data are consistent with most deformation occurring at temperatures of 500°C–600°C, with the structurally higher samples deforming at colder conditions in the 400°C–500°C range. In a study at Secret Creek gorge, Hacker et al. (1990) inferred peak mylonitization temperatures of ~630°C based on unpublished data from Hurlow, 1987's thesis. However, Hurlow et al. (1991) subsequently suggested temperatures of ~600°C. Therefore, based on constraints from this study and Hacker et al. (1990), we assume the highest temperature mylonitic shearing occurred at ~600°C but also acknowledge that our study did not employ quantitative methods.

5.2. Flow Stress and Strain Rate

The mylonitic rocks displayed recrystallized grainsizes ranging from 3 to 84 μm, which are approximately inversely correlated with structural depth, and corresponded to flow stress estimates of 209–28 MPa, respectively (Table 2; Figure 10). As expected for normal-sense exhumation of a broad brittle-ductile transition and our understanding of power-law rheology, the structurally higher samples reflect greater strength whereas the deeper samples are weaker (Behr & Platt, 2011). Although the temperature is only qualitatively determined, and any presumed geothermal gradient may become compressed during extension (e.g., England & Thompson, 1984; Ketcham, 1996; Marotta et al., 2009), our observations are consistent with the structurally higher samples being colder and stronger, and vice versa. For a temperature range of ~500°C–600°C and wet quartzite dislocation creep parameters (Hirth et al., 2001; Tokle et al., 2019), grainsize piezometry implies fast strain rates of $>10^{-13}$ s^{-1}.

5.3. Timing Constraints for Normal-Sense Shearing in the East Humboldt Range

Most penetrative fabrics in the East Humboldt Range consisted of subhorizontal to gently dipping foliations and west-northwest trending lineation that display top-west shear kinematics. However, rare top-east kinematics were also observed, generally at structurally deeper levels, and it is assumed that older Mesozoic top-east fabrics in this region were obliterated by top-west-northwest normal-sense shearing (McGrew, 1992, 2018; McGrew & Casey, 1998). Subtly deformed Tmg crosscutting mylonitic quartzite at a structurally deep locality near Steele Lake (Figure 6) is evidence for a pre-Oligocene phase of shearing. This older phase of deformation may have potentially attenuated some of the stratigraphy and condensed structural levels (Long & Kohn, 2020; McGrew et al., 2000), as quantified by thermobarometry data sets (Hallett & Spear, 2014, 2015). The relative contributions of Mesozoic vs. Cenozoic attenuation are impossible to quantify. In this regard, we discuss the more recent mylonitic episode, but emphasize that there was probably Jurassic and Cretaceous deformation (e.g., Hallett & Spear, 2015; Hudec, 1992; Jones, 1999; McGrew et al., 2000) that was overprinted by Cenozoic mylonitic shearing in the East Humboldt Range.

Direct crosscutting relationships with dated igneous rocks allow for the main phase of mylonitic shearing to span ca. 29 Ma (i.e., deformed Tmg) to ca. 17 Ma (i.e., undeformed subvertical basalt dikes; Snoke, 1980; Premo et al., 2014; Wright & Snoke, 1993; Zuza, Dee, et al., 2021; Zuza, Henry, et al., 2021; this study). To further resolve the timing of this deformation, we consider the two known geologic events between 29 and 17 Ma that could have driven mylonite formation: (a) deformation related to, or driven by, Oligocene magmatism (see Konstantinou et al., 2012, 2013 models for the Albion-Raft River-Grouse Creek MCC) or (b) the earliest phase of Miocene-to-present regional extension (bracketed to initiate at ca. 17–16 Ma; Colgan & Henry, 2009) that would have immediately preceded ca. 16.8 Ma basalt intrusions. As discussed above, mylonitic shearing was probably rapid (< several Myr), which means that it could have reflected initial hot and fast Miocene extension (e.g., Zuza et al., 2019) just prior to 17 Ma. However, ca. 17–15 Ma $^{40}Ar/^{39}Ar$ plagioclase phenocryst or plagioclase-bearing groundmass dates from Tb dikes around Angel Lake (Zuza, Henry, et al., 2021) imply that the dikes were cooled below plagioclase closure temperatures of ~225°C–300°C (e.g., Cassata et al., 2009) at this time. It is untenable that relatively hot quartz dynamic recrystallization temperatures (around 500°C–600°C; Hacker et al., 1990; this study) would cool that rapidly (<1 Myr) by ca. 17 Ma.

Conversely, a hypothesis of middle-late Oligocene shearing is supported by fission track and $^{40}Ar/^{39}Ar$ biotite dating that suggest cooling through ~300°C–200°C by ca. 23 Ma (Dokka et al., 1986; McGrew & Snee, 1994; Wright & Snoke, 1993) and observations of presently undated but undeformed mylonite-crosscutting leucogranite dikes in the East Humboldt Range (Figure 5c). Howard et al. (2011) reported ca. 29 Ma leucogranite in the Ruby Mountains to the south, and thus leucogranite with Oligocene ages are permissible. No Miocene leucogranites have been reported for the area, which leads us to interpret a probable Oligocene age for these dikes. Oligocene intrusions are not reported elsewhere in northern Nevada, outside of the Ruby Mountains-East Humboldt Range, and therefore we interpret that these localized intrusions are associated with the relatively local strong mylonitic shearing and pronounced exhumation of mid-crustal rocks observed in the East Humboldt Range. These lines of evidence suggest that the pervasive shear zone formed in the Oligocene, with late stages generating small volume leucogranite during decompression or dehydration melting. Future dating attempts on these crosscutting leucogranite dikes could provide better constraints.

The Ruby Mountain-East Humboldt Range detachment fault must have slipped after ca. 16.8 Ma, because the fault cuts basalt dikes of this age (Snoke, 1980; Zuza, Henry, et al., 2021). The simplest interpretation is that the main detachment initiated during the regional initiation of Basin and Range extension across Nevada at 17–16 Ma (Colgan & Henry, 2009), which is consistent with low-temperature apatite fission track and (U-Th)/He thermochronology from the southern Ruby Mountains that shows ca. 17–15 Ma cooling (Colgan et al., 2010) and the initial deposition of the syn-extensional Humboldt Formation. Available constraints allow detachment slip to have possibly occurred during Oligocene mylonitic shearing, either kinematically coupled with the mylonitic shear zone to generate brittle normal faults in the upper crust or as a structure to maintain strain compatibility between the high-strain mylonites and lesser deformed upper plate (e.g., J. Lee et al., 2017; E. L. Miller et al., 1983). However, we interpret the lack of syn-kinematic Oligocene basin deposits (Figure 1c) as evidence against significant Oligocene normal faulting.

5.4. Original Geometry of the Mylonitic Shear Zone and Detachment

The Ruby Mountain-East Humboldt Range detachment fault is subparallel to the underlying mylonitic shear zone (Haines & van der Pluijm, 2010; Hurlow, 1987; Hurlow et al., 1991; Snoke et al., 1997). Our data suggests that the lower plate largely consists of a relatively intact, coherent stratigraphic sequence from Zmu up to Oe, with structurally higher, finely recrystallized Mississippian siliciclastic rocks observed south in Secret Valley (e.g., Snoke et al., 2021). This stratigraphic thickness would have originally been ∼3.5 km (i.e., based on regional stratigraphy in Coats, 1987; Colgan et al., 2010; Zuza, Henry, et al., 2021), which was attenuated to a present-day thickness of ∼700 m (Figure 7a). This represents 80% vertical attenuation.

Alternatively, our interpretation of thrust duplication of Ordovician rocks over Mississippian strata as observed in the field (Figure 2a) and discussed above may imply more complex unit attenuation (Figure 7). In this case, the bulk geometries imply ∼87% attenuation (i.e., 5.5 km structural thickness thinned to ∼700 m; Figure 7b). This scenario implies a potential for heterogenous unit omission, and although some of the bulk attenuations could have been accomplished via normal-fault excision, our observations support that it mostly resulted from bulk structural attenuation. Namely, (a) there are no observations of fault structures cutting down section as expected for discrete normal faults and (b) individual distinct units were attenuated a comparable amount, such as Oe that was observed with ≤5 m thickness (Figure 5b) compared to a normal thickness of 50–70 m in adjacent ranges (Zuza et al., 2021), which equals >90% attenuation of the quartzite unit. This attenuation may have occurred entirely in the Oligocene, or as discussed above, it may represent the integrated history of Mesozoic and Cenozoic attenuation. Deformation of Oligocene granites requires that some of this attenuation occurred during or after the Oligocene. As a comparison, the northern Snake Range metamorphic core complex (Figure 1a) involved similar attenuation of the same stratigraphy (E. L. Miller et al., 1983) and available evidence suggests this occurred entirely in the Oligocene (J. Lee et al., 1987, 2017), which is consistent with our interpretation of predominately Oligocene attenuation in the East Humboldt Range.

Seemingly at odds with simple structural attenuation are the isoclinal folds nappes, such as the Winchell Lake fold nappe (Figure 2). In this study, new detrital zircon ages and carbon isotope confirmed age assignments from McGrew (2018), such that the southern nose of the nappe involves overturned isoclinal, recumbent folding of ЄZpmi through Mc. Our mapping supports that this structure was faulted over the main ЄZpmi-OЄmi units of the Tent Mountain quadrangle (west-striking fault north of Ackler Creek in Figure 2). McGrew (2018) and McGrew et al. (2000) argued that this nappe formed in the Late Cretaceous based on ca. 83–85 Ma leucogranite that was folded within the nose of the nappe, although MacCready et al. (1997) argued that similar recumbent folds and nappes in the Ruby Mountains formed in the Cenozoic during regional extension and associated crustal flow. The northward opening, isoclinal recumbent Winchell Lake synclinal nappe is somewhat incompatible with generation during predominately Mesozoic southeast-directed shortening (e.g., Zuza, Henry, et al., 2021), and its opposite vergence of Ruby Mountain nappes (MacCready et al., 1997) may support generation during buoyant diapirism as envisioned by Howard (1980, p. 345).

We hypothesize three scenarios where the Winchell Lake isoclinal fold may at least partially result from Cenozoic deformation (Figure 8b). First, it may result from attenuation of a more open, originally Mesozoic fold (i.e., 80% attenuation greatly exaggerating a preexisting fold; Figure 8b). Second, diapiric rise of the mid-lower crust, such as in the numerical models of Rey et al. (2017), could lead to local tight folding and overturning (Figure 8b; e.g., Dirks et al., 1997). Lastly, the fold nappe may result from a range-scale *a*-type fold (Sander, 1930; Figure 8b), as discussed by Malavielle (1987) in the Albion-Raft River-Grouse Creek (ARG) MCC. The parallelism between the isoclinal fold hinge and regional lineations suggest an *a*-type fold mechanism (e.g., Malavieille, 1987). All three mechanisms may be overprinting, such that earlier fold geometries were modified by diapiric flow and shearing (e.g., Dirks et al., 1997; Teyssier & Whitney, 2002). With these interpretations, we argue that this folding was complexly related to shearing and unit attenuation, at least partly during the Oligocene.

We can refine the pre-late Cenozoic orientation of the main mylonitic shear. In the southern East Humboldt Range, the coherent but attenuated mylonitic section dips ∼10°–15° west with shallowest subhorizontal dips near the range crest (Figure 13a). Detachment faulting and high-angle normal faulting would have potentially tilted the range. The subparallel Oe through Zmu units suggest this entire sequence was tilted together. In the simplest scenario, west-directed detachment faulting (Dokka et al., 1986; Hurlow et al., 1991) would have tilted the range eastward (e.g., Wernicke & Axen, 1988). The Quaternary high-angle faulting history is also consist-

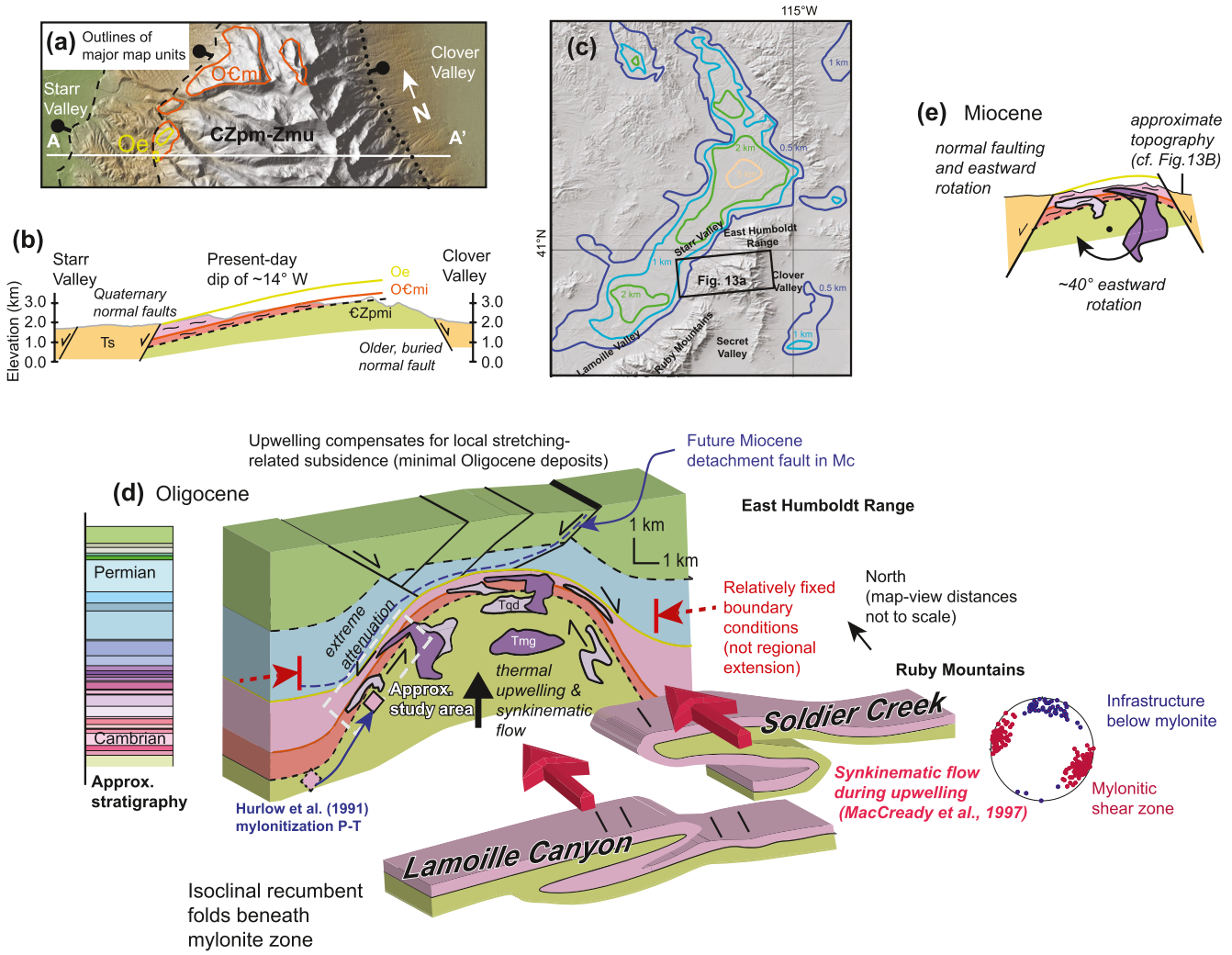

Figure 13. Sketch diagrams showing how the present-day geometry of the East Humboldt Range mylonitic shear zone relates to a plausible tectonic model for its Oligocene formation. (a) Digital elevation modelof the study area showing distribution of main Oe, O€m, and CZpmi-Zmu exposures (e.g., Figure, 2), topographic and section profile in (b), and range-bounding normal faults. The eastern fault is largely covered and less active, although the eastward range escarpment is steep. (b) Schematic cross-section along A-A' in (a) showing broad structure and shallow west dip of the mylonitic shear zone as exposed today. (c) Thickness of Cenozoic basins bounding the East Humboldt Range, inverted from gravity data (Ponce et al., 2011). Outline of (a) shown. (d) Model for buoyant upwelling and generation of a general-shear mylonite zone at a relatively steep angle with extreme unit attenuation. Minor upper crust extension may have occurred, resulting in precursor detachment-fault geometries that were balanced by upwelling so that Oligocene basin development was negligible. Later Miocene extension probably linked to this established shear zone (blue dashed line). Isoclinal recumbent folds in the Ruby Mountains partially accommodate northward crustal flow under this doming system (MacCready et al., 1997) based on north-trending lineations below the main mylonite zone and NW-trending lineations within the mylonite (see stereonet plot). The Lamoille and Solider Creek fold nappes are labeled to schematically show how they accommodate northward flow. (d) Middle Miocene-present high-angle normal faulting rotating the range ~40° east, predominately via slip on the western west-dipping range-bounding normal fault with lesser slip on the eastern range-bounding normal fault. This rotation results in a shear zone geometry that matches today, as compared with (b).

ent with eastward tilt. The western range front is bound by two active fault systems with prominent scarps in surficial deposits consistent with on-going Quaternary activity and bedrock exhumation (Figure 2). Late Pleistocene slip rates on the westernmost active fault with Holocene scarps are 0.1–0.2 mm yr^{-1} (Wesnousky & Willoughby, 2003; this study). Because the total exhumation rate is the sum of all active fault systems, the integrated slip rate of both fault systems is equal to, or greater than, this rate. Conversely, the eastern range-front fault system is weakly expressed by discontinuous, small fault scarps that appear less recently active with a minimal contribution to Quaternary range exhumation (Figure 13a). The thick Eocene-Miocene sedimentary basin on the west side of the East Humboldt Range suggests that faults on the westside have been more significant in creating accommodation space for sedimentation and adjacent range uplift (e.g., Colgan et al., 2010; Satarugsa & Johnson, 2000). Inversion of gravity data shows basins on the west side of the East Humboldt Range-Ruby Mountains

are >2 km deep, whereas Clover Basin on the east side of the East Humboldt Range is more sporadic and <1 km thick (Ponce et al., 2011; Figure 13c).

As an analog comparison, the Pequop Mountains experienced 40° of eastward rotation accommodated by west-dipping range-bounding normal faults and an early phase of detachment faulting (Zuza, Henry, et al., 2021). Geometric arguments show that Miocene eastward range tilting exhumed the bedrock in the Pequop Mountains from ~6 to 8 km depth, accompanied by syn-kinematic deposition of ~2 km of Miocene sediments along the western flank of the range (Zuza, Henry, et al., 2021). Furthermore, displaced late Pleistocene fans along the western flank of the Pequop Mountains (Figure 1) suggest 0.16 mm yr^{-1} vertical fault separation rates (Zuza, Henry, et al., 2021), which are comparable to the East Humboldt Range fault rates. The Humboldt Formation west of the East Humboldt Range is up to 5 km thick (Ponce et al., 2011; Satarugsa & Johnson, 2000), thicker than the Humboldt Formation in the Pequop Mountains. Therefore, we interpret the East Humboldt Range was tilted at least as much as the Pequop Mountains, or at least ~40° eastward since the Miocene. A low-temperature thermochronology traverse in the Ruby Mountains interpreted ~40° eastward tilting over this time period (Colgan et al., 2010). Following this logic, the East Humboldt Range mylonitic shear zone can be restored back to a ~55° west dip prior to range tilting (Figures 13b and 13e). We acknowledge the uncertainty in this estimate, which could have been shallower if the East Humboldt Range was tilted less due to competing fault activity on the eastern range-bounding fault, and therefore a range of 40°–55° original west dip is preferred. However, these geometries suggest that rocks exposed in the East Humboldt Range today were at depths of at least ~6 km prior to range tilting.

In addition, this geometric restoration implies that the mylonite-parallel Miocene detachment fault system initiated at similar moderate dips (40°–55°W), which simplifies issues of the mechanical feasibility of apparently low-angle normal faults (e.g., Axen, 2004; Collettini, 2011). That is, although the East Humboldt Range detachment fault currently has a shallow (≤10°W) orientation (e.g., Haines & van der Pluijm, 2010; Snoke, 1980) that would be mechanically unfavorable to initiate, our geometric restoration suggests that this normal fault initiated at more moderate dips due to pre-detachment-slip structural complexities.

5.5. General-Shear Stretching of the East Humboldt Range

No systematic variations in strain conditions (i.e., fabric strength or kinematics) were observed for different structural levels in the main mylonite. Deformation conditions are broadly compatible with structurally higher samples deforming at colder temperatures and higher stresses. We interpret this to suggest that from Oe down through ЄZpm, the entire section deformed as a homogenous shear zone without significant, focused strain partitioning. Crystallographic vorticity axis plots validate plane strain (Supporting Information). Some shear-zone attenuation may have occurred prior to the Oligocene, but because penetrative fabrics are developed in Oligocene granites and the older host rock, it is clear that at least some (or all) of this attenuation occurred in the Oligocene. We interpret that the severe attenuation of the mylonitic shear zone that is strongly lineated and displays pervasive top-west shear kinematics implies simultaneous contributions of pure- and simple-shear as general shear (or sub-simple shear). Simpson and De Paor (1993) discussed cases of general shear, and highlighted that the bounding wallrock of the general shear zone must be deformable or be separated from the shear zone by a fault structure. In this case, we argue that both situations are likely to occur in the East Humboldt Range, as the overlying upper Paleozoic rocks comprise a detachment fault system above the attenuated lower plate mylonitic shear zone. With a deformable wallrock, this shear zone system is defined as a stretching fault (Means, 1989).

Using bulk shear-zone attenuation observations to interpret the integrated strain history of this MCC inherently has some limitations, but we can place some preliminary bounds on shear-zone stretching. Assuming 2D conditions with no volume change, ~80% vertical shortening of the section (i.e., $-0.8\ \varepsilon_{yy}$) equates to 400% horizontal strain (i.e., $4\ \varepsilon_{xx}$) or 5× stretch, $S_x = \varepsilon_{xx} + 1$. Therefore, the rocks between ЄZpm and Oe may have been stretched ~5× their original length during vertical attenuation of ~80%. With this example, ~5 km of horizontal stratigraphy could be stretched to a length of ~25 km. Out-of-plane stretching (i.e., north-south) is possible, although our crystallographic vorticity axis observations suggest predominately plane strain monoclinic flow.

5.6. Interpretation of Cenozoic Tectonic History for the East Humboldt Range

Most published models for the Cenozoic evolution of the East Humboldt Range suggest that regional extension drives upper-crust normal faulting that was kinematically linked downdip with a mylonitic shear zone, with footwall exhumation driven by isostatic rebound during progressive hanging wall removal (e.g., Haines & van der Pluijm, 2010; Hurlow et al., 1991; MacCready et al., 1997). These models often invoke regional extension and detachment faulting from the Eocene to the mid-late Miocene, which predicts (a) a relatively long phase of continuous (or pulsed) extension at relatively moderate strain rates (10^{-14}–10^{-15} s^{-1}; e.g., Haines & van der Pluijm, 2010), (b) kinematic coupling between the upper crust faults and mylonitic shearing, (c) simple-shear strain in the mylonites (e.g., Davis, 1983), and (d) syn-kinematic basin records that match this extensional history (e.g., Dorsey & Becker, 1995; Friedmann & Burbank, 1995; Henry et al., 2011).

Observations from this study are not consistent with this aforementioned model because (a) microstructural data suggests faster strain rates of $>10^{-13}$ s^{-1} (Hacker et al., 1990; this study), (b) field and microstructure data favor strong vertical attenuation of the mylonitic shear zone, suggesting a strong component of pure shear, (c) there appears to be temporal decoupling between Oligocene mylonitic shearing and mid-Miocene detachment faulting, and (d) syn-kinematic basins only include a thin Eocene basin and more widespread and thicker Miocene basins. As mentioned above, current observations are ambiguous as to whether the East Humboldt Range records Eocene-Oligocene extension, but regional records suggest that pervasive regional extension in northeast Nevada did not commence until the middle Miocene (e.g., Colgan & Henry, 2009; Henry et al., 2011). The high horizontal stretch values (∼5×) implied by Oligocene attenuation of the mylonitic shear zone suggests that if this shear zone represented the down-dip continuation of an Oligocene brittle detachment fault, there should be substantial fault slip and thus an appreciable record of syn-kinematic basin sedimentation.

In light of observations from this study, integrated with interpretations from adjacent MCCs, we propose the following model for the Cenozoic evolution of the East Humboldt Range. Our tectonic model starts with the McCoy Creek Group rocks situated at ∼12–14 km depth based on *P-T* estimates of mylonitization (i.e., 3.1–3.7 kbar; Hurlow et al., 1991; Figure 13d). This implies that the rocks were near, or slightly deeper than, their original stratigraphic depths (∼10–15 km; Coats, 1987; Zuza, Henry, et al., 2021; Zuza et al., 2020, 2022). Our model is based on the following main observations and interpretations: (a) rapid shearing just after Oligocene magmatism as constrained by strain rates, previously published thermochronology (Dokka et al., 1986; McGrew & Snee, 1994; Wright & Snoke, 1993), and cross-cutting ca. 17 Ma basalt dikes; (b) an initially moderate-steepness geometry (∼40°–55° west) for the mylonite zone as inferred by late Cenozoic, post-mylonitization eastward rotation of the range (Figure 13), (c) a significant component of pure-shear stretching of the mylonitic shear zone (i.e., general shear); (d) the lack of Oligocene basin deposits (Lund Snee et al., 2016; Zuza, Henry, et al., 2021), which would be expected from regional Oligocene extension at this time (e.g., Dorsey & Becker, 1995; Friedmann & Burbank, 1995), (e) parallelism between Oligocene mylonitic shearing and Miocene detachment faulting (e.g., Dokka et al., 1986), and (f) a lack of substantial section omission across the detachment faults and mylonitic shear zone (Hurlow, 1987; Zuza, Dee, et al., 2021). Therefore, we find that (a) Oligocene mylonitic shearing coherently attenuated the existing stratigraphy, (b) Oligocene deformation was temporally decoupled from Miocene-present extension, and (c) the mylonitic shear zone was later tilted east to its present-day configuration. Our interpretations of pervasive general-shear stretching are most consistent with intrusion-related upward flow of the middle and lower crust, as envisioned by Konstantinou et al. (2012, 2013) for the ARG MCC (Figure 1a).

Mesozoic shortening may have resulted in some folding and unit duplication, including precursor folding and nappe development (e.g., McGrew et al., 2000) or the thrust emplacement of Ordovician rocks over Mississippian strata (Figure 7). Eocene magmatism generated extensive mantle-derived Tqd intrusions across the East Humboldt Range and Ruby Mountains, which was also expressed as coeval and genetically related volcanism (e.g., Henry et al., 2011; Howard, 2003; Lund Snee et al., 2016). Eocene volcanic rocks infilled paleovalleys but surface-breaking normal faulting and extension was minor (e.g., Cassel et al., 2018; Henry, 2018; M. E. Smith et al., 2017). The Eocene Cordilleran hinterland may have been extremely hot, potentially supporting higher surface elevations (Lund Snee et al., 2022). Konstantinou et al. (2013) argued that in the ARG, Eocene mantle-derived intrusions in the lower crust led to protracted heating, thermal incubation, and melt hybridization that generated Oligocene plutons with no record of coeval volcanism. We posit that the magmatic and thermal history in the East Humboldt Range may have been similar to the ARG, where Eocene quartz diorite intrusions drove remelting of the lower crust to generate voluminous, often leucocratic, Oligocene plutons in the

East Humboldt Range and Ruby Mountains (e.g., Howard et al., 2011; this study) with no volcanic equivalent. Geochronologic and petrologic investigations of magmatism at structurally deeper levels in the Ruby Mountains reveal a complex history of partial remelting and remobilization of Cretaceous and early Cenozoic granites (Howard et al., 2011) and continued investigations will lead to more insights to test our working hypothesis.

Regardless of origin, there is a striking spatial relationship in the region between significant Oligocene magmatism and mylonitic shearing, as Oligocene intrusions are not observed outside of the East Humboldt Range-Ruby Mountains except to the north in the ARG. The lack of Oligocene plutons elsewhere could be a unique exposure bias, but other ranges in the eastern Great Basin that expose stratigraphically deep Neoproterozoic through middle Paleozoic strata have no reported Oligocene plutons (e.g., the Pilot Range in northwest Utah; D. M. Miller, 1984). We, therefore, interpret this relationship to imply that the mylonitic shearing in the East Humboldt Range was be primarily driven by Oligocene magmatism. We argue that the hot and voluminously intruded middle crust rose buoyantly (e.g., Howard, 1980), which resulted in extreme attenuation of the upper crust and the Neoproterozoic-Paleozoic stratigraphy (e.g., Figure 13d). This thinning is analogous to how Cambrian strata were pure-shear attenuated around the Papoose Flat pluton in the White Mountain, eastern California, which coherently thinned the local section from ~1.2 km to ~100 m (e.g., Sylvester et al., 1978). Additionally, systematic study of pluton emplacement of the Fangshan pluton, China, shows pure-shear attenuation of the wallrock during the intrusion process (He et al., 2009; Zhao & Cong, 2014). Similarly, the East Humboldt Range may represent a magmatic gneiss dome. Density inversions as Rayleigh-Taylor instabilities can allow for diapiric rise of hotter and less dense middle-lower crust (e.g., Fletcher, 1972; Gilbert & Merle, 1987; Ramberg, 1981; Rey et al., 2009). It is possible that the rising gneiss dome could have generated, or substantially modified, the recumbent fold structures (e.g., Howard, 1980; Rey et al., 2017) in the region (Figure 8b).

During upwelling, a mobile lower crust may have flowed into the MCC (e.g., Gans, 1987; McKenzie et al., 2000), thus generating the Lamoille Canyon and Soldier Creek fold nappes and north-trending lineations observed in the central Ruby Mountains (MacCready et al., 1997; Figure 13d). Specifically, MacCready et al. (1997) interpreted that these northward flow structures were generated in the Oligocene based on strong north-trending lineations developed in ca. 29 Ma monzogranite, but McGrew et al. (2000) interpreted the fold nappes to have been generated during the Late Cretaceous. As discussed above, it is likely that earlier structures were overprinted by Oligocene deformation.

Minor decompression melting may explain the late-stage leucogranites observed cross-cutting mylonitic fabrics (e.g., Figures 5c and 5d). Thermal upwelling of the middle-lower crust would have compensated crustal subsidence implied by extreme attenuation, such that little space was generated for basin sedimentation. The Clover Creek stratigraphy (McGrew & Snoke, 2015; Zuza, Henry, et al., 2021) suggests that some thin Oligocene deposits (Figure 1c) could have been deposited at this time, or just after, but there were no significant Oligocene extensional basins (cf. Friedmann & Burbank, 1995). Miocene-present extension generated thick and widespread basins (e.g., Camilleri et al., 2017; Colgan & Henry, 2009; Henry et al., 2011; Satarugsa & Johnson, 2000; Zuza, Henry, et al., 2021). Mylonitic attenuation was decoupled from brittle upper crustal deformation, although some precursor low-angle detachment faulting may have occurred due to maintain upper vs. lower-plate strain compatibility (Figure 13d). The lack of significant stratigraphic omission across the detachment faults and mylonitic shear zone further support significant pure-shear stretching in this domal upwelling model (e.g., E. L. Miller et al., 1983).

Crustal attenuation at rapid strain rates $>10^{-13}$ s^{-1} could result in 400% horizontal stretching in ~1.3 Myr. Therefore, upwelling and attenuation may have been complete about a million years after ca. 29 Ma Tmg intrusions, which is consistent with fission track, $^{40}Ar/^{39}Ar$ biotite ages that suggest the rocks were cooled through ~300°C–200°C by ca. 23 Ma (Dokka et al., 1986; McGrew & Snee, 1994; Wright & Snoke, 1993). Regional Miocene detachment faulting starting at ca. 17 Ma (e.g., Colgan & Henry, 2009; Zuza et al., 2021) may have exploited the structural framework established by thermal upwelling, which was followed by high-angle normal faulting, Miocene basin deposition, and range tilting that impacted northeastern Nevada (e.g., Colgan & Henry, 2009; Zuza, Henry, et al., 2021; Figure 13d). This rotated the East Humboldt Range mylonitic shear zone to shallowly west dipping (Figure 13e).

6. Conclusions

In this study, we integrated new geologic mapping, geochronology, carbon isotope analyses, and microstructural observations across the East Humboldt Range metamorphic core complex, northeast Nevada, to constrain the style, timing, and magnitude of mylonitic shearing and crustal attenuation. We developed the following conclusions:

1. The top-west East Humboldt Range mylonitic shear zone deformed at strain rates $>10^{-13}$ s^{-1} at temperatures high enough for plastic quartz and feldspar dynamic recrystallization, probably 500°C–600°C, as evidenced by microstructural observations, quartz piezometry, and EBSD data.
2. Within the main mapped shear zone, there was no observed variation of strain with vertical structural position, other than expected higher stress conditions at structurally higher and colder levels. Field observations demonstrate a largely coherent original stratigraphy that was vertically attenuated at least 80%. Therefore, we interpret the East Humboldt Range mylonites as having formed as a general-shear zone.
3. Direct cross-cutting relationships require mylonitic shearing between ca. 29 and 16.8 Ma, but we further interpret that this deformation occurred contemporaneously, or shortly after, Oligocene magmatism. The mylonite is cross-cut by leucogranite dikes of unknown age (probably Oligocene) and middle Miocene basalt dikes.
4. The East Humboldt Range mylonite zone probably rotated eastward due to Miocene normal faulting, as observed for most other ranges in the area. This geometric consideration implies that the shear zone formed at a steeper dip than today (~40°–55° west).
5. Taken together, the timing and nature of this general shear zone is consistent with its formation during Oligocene thermal upwelling and doming, as envisioned for the Albion-Raft River-Grouse Creek MCC in Utah to the northeast. Therefore, we argue that this mylonitic shear zone did not accommodate regional extension, which is consistent with the lack of syn-extensional Oligocene basin deposits and prevalence of clear Miocene extensional basins that mark the onset of regionally significant Basin and Range extension in northeast Nevada.

Data Availability Statement

All data presented in this study are available in the Supporting Information File. Geochronology and geochemistry data have been archived in the Earthchem data repository at http://doi.org/10.26022/IEDA/112276 and http://doi.org/10.26022/IEDA/112278, respectively.

Acknowledgments
This research was supported by the USGS National Cooperative Geologic Mapping Program via State Map awards (G19AC00383, G20AS00006), National Science Foundation Tectonics program (EAR, 1830139), and the Geological Society of Nevada. The Arizona LaserChron Center is supported by the National Science Foundation (EAR 1649254). The authors thank Art Snoke for showing us the geology of the East Humboldt Range, aiding our geologic mapping, and reviewing some of the important unanswered questions. Chuck Thorman and Chris Henry are thanked for discussions on the geology of northeast Nevada. Constructive editorial handling and review comments by Editor Margaret Rusmore, the Associate Editor, Tom Hoisch, and Sean Long greatly improved this paper. Stacia Gordon collected sample RH 12-03.

References

Armstrong, R. L. (1982). Cordilleran metamorphic core complexes-from Arizona to southern Canada. *Annual Review of Earth and Planetary Sciences*, *10*, 129–154. https://doi.org/10.1146/annurev.ea.10.050182.001021

Axen, G. J. (2004). Chapter 3. Mechanics of low-angle normal faults. In *Rheology and deformation of the lithosphere at continental margins* (pp. 46–91). Columbia University Press. https://doi.org/10.7312/karn12738-004

Axen, G. J. (2020). How a strong low-angle normal fault formed: The Whipple detachment, southeastern California. *Bulletin*, *132*(9–10), 1817–1828. https://doi.org/10.1130/b35386.1

Axen, G. J., van Wijk, J. W., & Currie, C. A. (2018). Basal continental mantle lithosphere displaced by flat-slab subduction. *Nature Geoscience*, *11*(12), 961–964. https://doi.org/10.1038/s41561-018-0263-9

Bachmann, F., Hielscher, R., & Schaeben, H. (2011). Grain detection from 2d and 3d EBSD data—Specification of the MTEX algorithm. *Ultramicroscopy*, *111*(12), 1720–1733. https://doi.org/10.1016/j.ultramic.2011.08.002

Bailey, C. M., & Eyster, E. L. (2003). General shear deformation in the Pinaleno Mountains metamorphic core complex, Arizona. *Journal of Structural Geology*, *25*(11), 1883–1892. https://doi.org/10.1016/s0191-8141(03)00044-0

Barth, N. C., Hacker, B. R., Seward, G. G., Walsh, E. O., Young, D., & Johnston, S. (2010). Strain within the ultrahigh-pressure Western Gneiss region of Norway recorded by quartz CPOs. *Geological Society, London, Special Publications*, *335*(1), 663–685. https://doi.org/10.1144/sp335.27

Bartley, J. M., & Wernicke, B. P. (1984). The Snake Range decollement interpreted as a major extensional shear zone. *Tectonics*, *3*(6), 647–657. https://doi.org/10.1029/tc003i006p00647

Batum, M. A. (1999). *Petrology of Late Cretaceous and Cenozoic granitic rocks, East Humboldt Range, northeastern Nevada, (Doctoral dissertation)*. Texas Tech University.

Behr, W. M., & Platt, J. P. (2011). A naturally constrained stress profile through the middle crust in an extensional terrane. *Earth and Planetary Science Letters*, *303*(3–4), 181–192. https://doi.org/10.1016/j.epsl.2010.11.044

Beranek, L. P., Link, P. K., & Fanning, C. M. (2016). Detrital zircon record of mid-Paleozoic convergent margin activity in the northern US Rocky Mountains: Implications for the Antler orogeny and early evolution of the North American Cordillera. *Lithosphere*, *8*(5), 533–550. https://doi.org/10.1130/l557.1

Best, M. G., Christiansen, E. H., de Silva, S., & Lipman, P. W. (2016). Slab-rollback ignimbrite flareups in the southern Great Basin and other Cenozoic American arcs: A distinct style of arc volcanism. *Geosphere*, *12*(4), 1097–1135. https://doi.org/10.1130/ges01285.1

Bestmann, M., & Prior, D. J. (2003). Intragranular dynamic recrystallization in naturally deformed calcite marble: Diffusion accommodated grain boundary sliding as a result of subgrain rotation recrystallization. *Journal of Structural Geology*, *25*(10), 1597–1613. https://doi.org/10.1016/s0191-8141(03)00006-3

Blumenfeld, P., & Bouchez, J. L. (1988). Shear criteria in granite and migmatite deformed in the magmatic and solid states. *Journal of Structural Geology*, *10*(4), 361–372. https://doi.org/10.1016/0191-8141(88)90014-4

Blumenfeld, P., Mainprice, D., & Bouchez, J. L. (1986). C-slip in quartz from subsolidus deformed granite. *Tectonophysics*, *127*(1–2), 97–115. https://doi.org/10.1016/0040-1951(86)90081-8

Bond, G. C., Kominz, M. A., Steckler, M. S., Grotzinger, J. P., & Crevello, P. D. (1989). Role of thermal subsidence, flexure, and eustasy in the evolution of early Paleozoic passive-margin carbonate platforms. *Controls on Carbonate Platform and Basin Development: SEPM, Special Publication*, *44*, 39–61. https://doi.org/10.2110/pec.89.44.0039

Brueseke, M. E., Callicoat, J. S., Hames, W., & Larson, P. B. (2014). Mid-Miocene rhyolite volcanism in northeastern Nevada: The Jarbidge Rhyolite and its relationship to the Cenozoic evolution of the northern Great Basin (USA). *Bulletin*, *126*(7–8), 1047–1067. https://doi.org/10.1130/b30736.1

Camilleri, P., Deibert, J., & Perkins, M. (2017). Middle Miocene to Holocene tectonics, basin evolution, and paleogeography along the southern margin of the Snake River Plain in the Knoll Mountain-Ruby-East Humboldt Range region, northeastern Nevada and south-central Idaho. *Geosphere*, *13*(6), 1901–1948. https://doi.org/10.1130/ges01318.1

Camilleri, P., Yonkee, A., Coogan, J., DeCelles, P., McGrew, A., & Wells, M. (1997). Mesozoic tectonics and metamorphism in the Pequop Mountains and Wood Hills region, northeast Nevada: Implications for the architecture and evolution of the Sevier orogen. *Geological Society of America Bulletin*, *109*(1), 74–94.

Cassata, W. S., Renne, P. R., & Shuster, D. L. (2009). Argon diffusion in plagioclase and implications for thermochronometry: A case study from the Bushveld Complex, South Africa. *Geochimica et Cosmochimica Acta*, *73*(21), 6600–6612. https://doi.org/10.1016/j.gca.2009.07.017

Cassel, E. J., Breecker, D. O., Henry, C. D., Larson, T. E., & Stockli, D. F. (2014). Profile of a paleo-orogen: High topography across the present-day Basin and Range from 40 to 23 Ma. *Geology*, *42*(11), 1007–1010. https://doi.org/10.1130/g35924.1

Cassel, E. J., Smith, M. E., & Jicha, B. R. (2018). The impact of slab rollback on earth's surface: Uplift and extension in the hinterland of the North American Cordillera. *Geophysical Research Letters*, *45*(20), 10–996. https://doi.org/10.1029/2018gl079887

Chamberlain, C. P., Mix, H. T., Mulch, A., Hren, M. T., Kent-Corson, M. L., Davis, S. J., et al. (2012). The Cenozoic climatic and topographic evolution of the western North American Cordillera. *American Journal of Science*, *312*(2), 213–262. https://doi.org/10.2475/02.2012.05

Chapman, J. B., Ducea, M. N., DeCelles, P. G., & Profeta, L. (2015). Tracking changes in crustal thickness during orogenic evolution with Sr/Y: An example from the North American Cordillera. *Geology*, *43*(10), 919–922. https://doi.org/10.1130/g36996.1

Coats, R. R. (1987). *Geology of Elko County, Nevada* (Vol. 101). Nevada Bureau of Mines and Geology, University of Nevada-Reno.

Colgan, J. P., & Henry, C. D. (2009). Rapid middle Miocene collapse of the Mesozoic orogenic plateau in north-central Nevada. *International Geology Review*, *51*(9–11), 920–961. https://doi.org/10.1080/00206810903056731

Colgan, J. P., Howard, K. A., Fleck, R. J., & Wooden, J. L. (2010). Rapid middle Miocene extension and unroofing of the southern Ruby Mountains, Nevada. *Tectonics*, *29*(6). https://doi.org/10.1029/2009tc002655

Collettini, C. (2011). The mechanical paradox of low-angle normal faults: Current understanding and open questions. *Tectonophysics*, *510*(3–4), 253–268. https://doi.org/10.1016/j.tecto.2011.07.015

Coney, P. J. (1980). Cordilleran metamorphic core complexes: An overview. *Cordilleran metamorphic core complexes* (Vol. 153, pp. 7–31). Geological Society of America Memoir. https://doi.org/10.1130/mem153-p7

Coney, P. J., & Harms, T. A. (1984). Cordilleran metamorphic core complexes: Cenozoic extensional relics of Mesozoic compression. *Geology*, *12*(9), 550–554. https://doi.org/10.1130/0091-7613(1984)12<550:cmccce>2.0.co;2

Copeland, P., Currie, C. A., Lawton, T. F., & Murphy, M. A. (2017). Location, location, location: The variable lifespan of the Laramide orogeny. *Geology*, *45*(3), 223–226. https://doi.org/10.1130/g38810.1

Crittenden, M. D., Coney, P. J., Davis, G. H., & Davis, G. H. (Eds.). (1980). *Cordilleran metamorphic core complexes* (Vol. 153). Geological Society of America Memoir.

Cross, A. J., Prior, D. J., Stipp, M., & Kidder, S. (2017). The recrystallized grainsize piezometer for quartz: An EBSD-based calibration. *Geophysical Research Letters*, *44*(13), 6667–6674. https://doi.org/10.1002/2017gl073836

Davis, G. H. (1983). Shear-zone model for the origin of metamorphic core complexes. *Geology*, *11*(6), 342–347. https://doi.org/10.1130/0091-7613(1983)11<342:smftoo>2.0.co;2

DeCelles, P. G. (2004). Late Jurassic to Eocene evolution of the Cordilleran thrust belt and foreland basin system, western USA. *American Journal of Science*, *304*(2), 105–168. https://doi.org/10.2475/ajs.304.2.105

DeCelles, P. G., & Coogan, J. C. (2006). Regional structure and kinematic history of the Sevier fold-and-thrust belt, central Utah. *The Geological Society of America Bulletin*, *118*(7–8), 841–864. https://doi.org/10.1130/b25759.1

Dee, S., Dering, G. M., & Henry, C. D. (2015). *Preliminary Geologic Map of the Herder Creek Quadrangle, Elko County, Nevada*, (p. 5). Nevada Bureau of Mines and Geology Open File Report 16-5, scale 1:24,000.

Dee, S., & Ressel, M. W. (2016). *Preliminary geologic map of the Heelfly Creek quadrangle and adjacent parts of the Tent Mountain, Soldier Peak, and Secret Valley quadrangles, Elko County, Nevada* (p. 5). Nevada Bureau of Mines and Geology Open File Report 15-4, scale 1:24,000.

Dickinson, W. R. (2004). Evolution of the North American cordillera. *Annual Review of Earth and Planetary Sciences*, *32*, 13–45.

Dirks, P. H. G. M., Zhang, J. S., & Passchier, C. W. (1997). Exhumation of high-pressure granulites and the role of lower crustal advection in the North China Craton near Datong. *Journal of Structural Geology*, *19*(10), 1343–1358. https://doi.org/10.1016/s0191-8141(97)00044-8

Dokka, R. K., Mahaffie, M. J., & Snoke, A. W. (1986). Thermochronologic evidence of major tectonic denudation associated with detachment faulting, northern Ruby Mountains-East Humboldt Range, Nevada. *Tectonics*, *5*(7), 995–1006. https://doi.org/10.1029/tc005i007p00995

Dorsey, R. J., & Becker, U. (1995). Evolution of a large Miocene growth structure in the upper plate of the Whipple detachment fault, northeastern Whipple Mountains, California. *Basin Research*, *7*(2), 151–163. https://doi.org/10.1111/j.1365-2117.1995.tb00101.x

England, P. C., & Thompson, A. B. (1984). Pressure-temperature-time paths of regional metamorphism II. Their inference and interpretation using mineral assemblages in metamorphic rocks. *Journal of Petrology*, *25*(4), 929–955. https://doi.org/10.1093/petrology/25.4.894

Faleiros, F. M., Moraes, R. D., Pavan, M., & Campanha, G. D. C. (2016). A new empirical calibration of the quartz *c*-axis fabric opening-angle deformation thermometer. *Tectonophysics*, *671*, 173–182. https://doi.org/10.1016/j.tecto.2016.01.014

Fletcher, R. C. (1972). Application of a mathematical model to the emplacement of mantled gneiss domes. *American Journal of Science*, *272*(3), 197–216. https://doi.org/10.2475/ajs.272.3.197

Fricke, H. C., Wickham, S. M., & O'Neil, J. R. (1992). Oxygen and hydrogen isotope evidence for meteoric water infiltration during mylonitization and uplift in the Ruby Mountains-East Humboldt Range core complex, Nevada. *Contributions to Mineralogy and Petrology*, *111*(2), 203–221. https://doi.org/10.1007/bf00348952

Friedmann, S. J., & Burbank, D. W. (1995). Rift basins and supradetachment basins: Intracontinental extensional end-members. *Basin Research*, *7*(2), 109–127. https://doi.org/10.1111/j.1365-2117.1995.tb00099.x

Gans, P. B. (1987). An open-system, two-layer crustal stretching model for the eastern Great Basin. *Tectonics*, *6*(1), 1–12. https://doi.org/10.1029/tc006i001p00001

Gehrels, G., & Pecha, M. (2014). Detrital zircon U-Pb geochronology and Hf isotope geochemistry of Paleozoic and Triassic passive margin strata of western North America. *Geosphere*, *10*(1), 49–65.

Gilbert, E., & Merle, O. (1987). Extrusion and radial spreading beyond a closing.

Hacker, B. R., Ratschbacher, L., Webb, L., McWilliams, M. O., Ireland, T., & Calvert, A. (2000). Exhumation of ultrahigh-pressure continental crust in east central China: Late Triassic-Early Jurassic tectonic unroofing. *Journal of Geophysical Research: Solid Earth*, *105*(B6), 13339–13364. https://doi.org/10.1029/2000jb900039

Hacker, B. R., Yin, A., Christie, J. M., & Snoke, A. W. (1990). Differential stress, strain rate, and temperatures of mylonitization in the Ruby Mountains, Nevada: Implications for the rate and duration of uplift. *Journal of Geophysical Research: Solid Earth*, *95*(B6), 8569–8580. https://doi.org/10.1029/jb095ib06p08569

Hadlari, T., Davis, W. J., Dewing, K., Heaman, L. M., Lemieux, Y., Ootes, L., et al. (2012). Two detrital zircon signatures for the Cambrian passive margin of northern Laurentia highlighted by new U-Pb results from northern Canada. *Bulletin*, *124*(7–8), 1155–1168. https://doi.org/10.1130/b30530.1

Haines, S. H., & van der Pluijm, B. A. (2010). Dating the detachment fault system of the Ruby Mountains, Nevada: Significance for the kinematics of low-angle normal faults. *Tectonics*, *29*(4). https://doi.org/10.1029/2009tc002552

Hallett, B. W., & Spear, F. S. (2014). The P-T history of anatectic pelites of the Northern East Humboldt Range, Nevada: Evidence for tectonic loading, decompression, and anatexis. *Journal of Petrology*, *55*(1), 3–36. https://doi.org/10.1093/petrology/egt057

Hallett, B. W., & Spear, F. S. (2015). Monazite, zircon, and garnet growth in migmatitic pelites as a record of metamorphism and partial melting in the East Humboldt Range, Nevada. *American Mineralogist*, *100*(4), 951–972. https://doi.org/10.2138/am-2015-4839

He, B., Xu, Y. G., & Paterson, S. (2009). Magmatic diapirism of the Fangshan pluton, southwest of Beijing, China. *Journal of Structural Geology*, *31*(6), 615–626. https://doi.org/10.1016/j.jsg.2009.04.007

Henry, C. D. (2008). Ash-flow tuffs and paleovalleys in northeastern Nevada: Implications for Eocene paleogeography and extension in the Sevier hinterland, northern Great Basin. *Geosphere*, *4*(1), 1–35. https://doi.org/10.1130/ges00122.1

Henry, C. D. (2018). The Eocene Elko Basin and Elko formation, NE Nevada: Paleotopographic controls on area, thickness, facies distribution, and petroleum potential. In *AAPG ACE 2018*.

Henry, C. D., Hinz, N. H., Faulds, J. E., Colgan, J. P., John, D. A., Brooks, E. R., et al. (2012). Eocene-Early Miocene paleotopography of the Sierra Nevada-Great Basin-Nevadaplano based on widespread ash-flow tuffs and paleovalleys. *Geosphere*, *8*(1), 1–27. https://doi.org/10.1130/ges00727.1

Henry, C. D., McGrew, A. J., Colgan, J. P., Snoke, A. W., Brueseke, M. E., Lee, J., & Evans, J. P. (2011). *Timing, distribution, amount, and style of Cenozoic extension in the northern Great Basin. Geologic field trips to the basin and range, Rocky Mountains, Snake River Plain, and Terranes of the US Cordillera* (Vol. 21, pp. 27–66). Geological Society of America Field Guide.

Hirth, G., Teyssier, C., & Dunlap, J. W. (2001). An evaluation of quartzite flow laws based on comparisons between experimentally and naturally deformed rocks. *International Journal of Earth Sciences*, *90*(1), 77–87. https://doi.org/10.1007/s005310000152

Hirth, G., & Tullis, J. (1992). Dislocation creep regimes in quartz aggregates. *Journal of Structural Geology*, *14*(2), 145–159. https://doi.org/10.1016/0191-8141(92)90053-y

Howard, K. A. (1966). *Structure of the metamorphic rocks of the northern Ruby Mountains, Nevada, (Ph.D. thesis)* (p. 170). New Haven: Yale University.

Howard, K. A. (1971). Paleozoic metasediments in the northern Ruby Mountains, Nevada. *The Geological Society of America Bulletin*, *82*, 250–264. https://doi.org/10.1130/0016-7606(1971)82[259:pmitnr]2.0.co;2

Howard, K. A. (1980). Metamorphic infrastructure in the northern Ruby Mountains, Nevada. In M. D. Crittenden, Jr., P. J. Coney, & G. H. Davis (Eds.), *Cordilleran metamorphic core complexes* (Vol. 153, pp. 335–347). Geological Society of America Memoir.

Howard, K. A. (2003). Crustal structure in the Elko-Carlin region, Nevada, during Eocene gold mineralization: Ruby-East Humboldt metamorphic core complex as a guide to the deep crust. *Economic Geology*, *98*(2), 249–268. https://doi.org/10.2113/gsecongeo.98.2.249

Howard, K. A., Wooden, J. L., Barnes, C. G., Premo, W. R., Snoke, A. W., & Lee, S. Y. (2011). Episodic growth of a Late Cretaceous and Paleogene intrusive complex of pegmatitic leucogranite, Ruby Mountains core complex, Nevada, USA. *Geosphere*, *7*(5), 1220–1248. https://doi.org/10.1130/ges00668.1

Hudec, M. R. (1992). Mesozoic structural and metamorphic history of the central Ruby Mountains metamorphic core complex, Nevada. *The Geological Society of America Bulletin*, *104*(9), 1086–1100. https://doi.org/10.1130/0016-7606(1992)104<1086:msamho>2.3.co;2

Hurlow, H. A. (1987). *Structural geometry, fabric, and chronology of a Tertiary extensional shear zone—Detachment system, (M.S. thesis)* (p. 140). Laramie: University of Wyoming.

Hurlow, H. A., Snoke, A. W., & Hodges, K. V. (1991). Temperature and pressure of mylonitization in a Tertiary extensional shear zone, Ruby Mountains-East Humboldt Range, Nevada: Tectonic implications. *Geology*, *19*(1), 82–86. https://doi.org/10.1130/0091-7613(1991)019<0082:tapomi>2.3.co;2

Ismaïl, W. B., & Mainprice, D. (1998). An olivine fabric database: An overview of upper mantle fabrics and seismic anisotropy. *Tectonophysics*, *296*(1–2), 145–157.

Jessell, M. W. (1987). Grain-boundary migration microstructures in a naturally deformed quartzite. *Journal of Structural Geology*, *9*(8), 1007–1014. https://doi.org/10.1016/0191-8141(87)90008-3

Jiang, Z., Prior, D. J., & Wheeler, J. (2000). Albite crystallographic preferred orientation and grain misorientation distribution in a low-grade mylonite: Implications for granular flow. *Journal of Structural Geology*, *22*(11–12), 1663–1674. https://doi.org/10.1016/s0191-8141(00)00079-1

Jones, J. V. (1999). *Deformational, magmatic, and metamorphic history of the central Ruby Mountains, Elko County, Nevada, (M.S. thesis)* (p. 166). Laramie: University of Wyomong.

Ketcham, R. A. (1996). Thermal models of core-complex evolution in Arizona and New Guinea: Implications for ancient cooling paths and present-day heat flow. *Tectonics*, *15*(5), 933–951. https://doi.org/10.1029/96tc00033

Ketner, K. B. (2008). The Inskip Formation, the Harmony Formation, and the Havallah sequence of northwestern Nevada—An interrelated Paleozoic assemblage in the home of the Sonoma Orogeny: U.S. *Geological Survey Professional Paper*, *21*, 1757. https://doi.org/10.3133/pp1757

Konstantinou, A., Strickland, A., Miller, E. L., Vervoort, J., Fisher, C. M., Wooden, J., & Valley, J. (2013). Synextensional magmatism leading to crustal flow in the Albion-Raft River-Grouse Creek metamorphic core complex, northeastern Basin and Range. *Tectonics*, *32*(5), 1384–1403. https://doi.org/10.1002/tect.20085

Konstantinou, A., Strickland, A., Miller, E. L., & Wooden, J. P. (2012). Multistage Cenozoic extension of the Albion-Raft River-Grouse Creek metamorphic core complex: Geochronologic and stratigraphic constraints. *Geosphere*, *8*(6), 1429–1466. https://doi.org/10.1130/ges00778.1

Laabs, B. J., Munroe, J. S., Best, L. C., & Caffee, M. W. (2013). Timing of the last glaciation and subsequent deglaciation in the Ruby Mountains, Great Basin, USA. *Earth and Planetary Science Letters*, *361*, 16–25. https://doi.org/10.1016/j.epsl.2012.11.018

Law, R. D. (2014). Deformation thermometry based on quartz *c*-axis fabrics and recrystallization microstructures: A review. *Journal of Structural Geology*, *66*, 129–161. https://doi.org/10.1016/j.jsg.2014.05.023

Lee, J., Blackburn, T., & Johnston, S. (2017). Timing of mid-crustal ductile extension in the northern Snake Range metamorphic core complex, Nevada: Evidence from U/Pb zircon ages. *Geosphere*, *13*(2), 439–459. https://doi.org/10.1130/ges01429.1

Lee, J., Miller, E. L., & Sutter, J. F. (1987). Ductile strain and metamorphism in an extensional tectonic setting: A case study from the northern Snake Range, Nevada, USA. *Geological Society, London, Special Publications*, *28*(1), 267–298. https://doi.org/10.1144/gsl.sp.1987.028.01.18

Lee, S. Y., Barnes, C. G., Snoke, A. W., Howard, K. A., & Frost, C. D. (2003). Petrogenesis of Mesozoic, peraluminous granites in the Lamoille Canyon area, Ruby Mountains, Nevada, USA. *Journal of Petrology*, *44*(4), 713–732. https://doi.org/10.1093/petrology/44.4.713

Lister, G. S., & Davis, G. A. (1989). The origin of metamorphic core complexes and detachment faults formed during Tertiary continental extension in the northern Colorado River region, USA. *Journal of Structural Geology*, *11*(1–2), 65–94. https://doi.org/10.1016/0191-8141(89)90036-9

Lloyd, G. E., & Freeman, B. (1994). Dynamic recrystallization of quartz under greenschist conditions. *Journal of Structural Geology*, *16*(6), 867–881. https://doi.org/10.1016/0191-8141(94)90151-1

Long, S. P. (2012). Magnitudes and spatial patterns of erosional exhumation in the Sevier hinterland, eastern Nevada and western Utah, USA: Insights from a Paleogene paleogeologic map. *Geosphere*, *8*(4), 881–901.

Long, S. P. (2019). Geometry and magnitude of extension in the Basin and Range Province (39°N), Utah, Nevada, and California, USA: Constraints from a province-scale cross-section. *GSA Bulletin*, *131*(1–2), 99–119. https://doi.org/10.1130/b31974.1

Long, S. P., & Kohn, M. J. (2020). Distributed ductile thinning during thrust emplacement: A commonly overlooked exhumation mechanism. *Geology*, *48*(4), 368–373. https://doi.org/10.1130/g47022.1

Lund Snee, J. E., & Miller, E. L. (2022). *Magmatism, migrating topography, and the transition from Sevier shortening to Basin and Range extension, western USA*. GSA Memoirs.

Lund Snee, J. E., Miller, E. L., Grove, M., Hourigan, J. K., & Konstantinou, A. (2016). Cenozoic paleogeographic evolution of the Elko Basin and surrounding region, northeast Nevada. *Geosphere*, *12*(2), 464–500. https://doi.org/10.1130/ges01198.1

MacCready, T., Snoke, A. W., Wright, J. E., & Howard, K. A. (1997). Mid-crustal flow during Tertiary extension in the Ruby Mountains core complex, Nevada. *The Geological Society of America Bulletin*, *109*(12), 1576–1594. https://doi.org/10.1130/0016-7606(1997)109<1576:mcfdte>2.3.co;2

Mainprice, D., Bachmann, F., Hielscher, R., & Schaeben, H. (2015). Descriptive tools for the analysis of texture projects with large data sets using MTEX: Strength, symmetry, and components. *Geological Society, London, Special Publications*, *409*(1), 251–271. https://doi.org/10.1144/sp409.8

Mainprice, D., Bascou, J., Cordier, P., & Tommasi, A. (2004). Crystal preferred orientations of garnet: Comparison between numerical simulations and electron back-scattered diffraction (EBSD) measurements in naturally deformed eclogites. *Journal of Structural Geology*, *26*(11), 2089–2102. https://doi.org/10.1016/j.jsg.2004.04.008

Mainprice, D., Bouchez, J. L., Blumenfeld, P., & Tubià, J. M. (1986). Dominant c slip in naturally deformed quartz: Implications for dramatic plastic softening at high temperature. *Geology*, *14*(10), 819–822. https://doi.org/10.1130/0091-7613(1986)14<819:dcsind>2.0.co;2

Malavieille, J. (1987). Extensional shearing deformation and kilometer-scale "a"-type folds in a Cordilleran metamorphic core complex (Raft River Mountains, northwestern Utah). *Tectonics*, *6*(4), 423–448. https://doi.org/10.1029/tc006i004p00423

Marotta, A. M., Spalla, M. I., & Gosso, G. (2009). Upper and lower crustal evolution during lithospheric extension: Numerical modeling and natural footprints from the European Alps. *Geological Society, London, Special Publications*, *321*(1), 33–72. https://doi.org/10.1144/sp321.3

Mattauer, M. (1975). Sur le mécanisme de formation de la schistosité dans l'Himalaya. *Earth and Planetary Science Letters*, *28*(2), 144–154. https://doi.org/10.1016/0012-821x(75)90222-8

McGrew, A. J. (1992). *Tectonic evolution of the northern East Humboldt Range, Elko County, Nevada, (Ph.D. dissertation)* (p. 191). Laramie: University of Wyoming.

McGrew, A. J. (2018). *Geologic map of the Humboldt Peak Quadrangle, Elko County, Nevada* (Vol. 186, p. 23). Nevada Bureau of Mines Map. 1:24,000 scale.

McGrew, A. J., & Casey, M. (1998). Quartzite fabric transition in a Cordilleran metamorphic core complex. In A. W. Snoke, J. A. Tullis, & V. R. Todd (Eds.), *Fault-related rocks—A photographic atlas* (pp. 484–489). Princeton, New Jersey: Princeton University Press. https://doi.org/10.1515/9781400864935.484

McGrew, A. J., & Peters, M. T. (1997). *Grand tour—Part 2: Petrogenesis and thermal evolution of deep continental-crust: The record from the East Humboldt Range* (p. 42). Nevada: Brigham Young University Geology Studies.

McGrew, A. J., Peters, M. T., & Wright, J. E. (2000). Thermobarometric constraints on the tectonothermal evolution of the East Humboldt Range metamorphic core complex, Nevada. *The Geological Society of America Bulletin*, *112*(1), 45–60. https://doi.org/10.1130/0016-7606(2000)112<45:tcotte>2.0.co;2

McGrew, A. J., & Snee, L. W. (1994). $^{40}Ar/^{39}Ar$ thermochronologic constraints on the tectonothermal evolution of the northern East Humboldt Range metamorphic core complex, Nevada. *Tectonophysics*, *238*(1–4), 425–450. https://doi.org/10.1016/0040-1951(94)90067-1

McGrew, A. J., & Snoke, A. W. (2015). Geologic map of the welcome quadrangle and an adjacent part of the wells quadrangle, Elko County, Nevada. *Nevada Bureau of Mines and Geology Map*, *184*(1), 40. 24,000 scale.

McKenzie, D., Nimmo, F., Jackson, J. A., Gans, P. B., & Miller, E. L. (2000). Characteristics and consequences of flow in the lower crust. *Journal of Geophysical Research: Solid Earth*, *105*(B5), 11029–11046. https://doi.org/10.1029/1999jb900446

McQuarrie, N., & Wernicke, B. P. (2005). An animated tectonic reconstruction of southwestern North America since 36 Ma. *Geosphere*, *1*(3), 147–172. https://doi.org/10.1130/ges00016.1

Means, W. D. (1989). Stretching faults. *Geology*, *17*(10), 893–896. https://doi.org/10.1130/0091-7613(1989)017<0893:sf>2.3.co;2

Michels, Z. D., Kruckenberg, S. C., Davis, J. R., & Tikoff, B. (2015). Determining vorticity axes from grain-scale dispersion of crystallographic orientations. *Geology*, *43*(9), 803–806. https://doi.org/10.1130/g36868.1

Miller, D. M. (1984). *Sedimentary and igneous rocks of the Pilot Range and vicinity* (pp. 45–63). Utah and Nevada. Geology of Northwest Utah, Southern Idaho and Northeast Nevada, Utah Geological Association.

Miller, D. M., & Hoisch, T. D. (1995). Jurassic tectonics of northeastern Nevada and northwestern Utah from the perspective of barometric studies. In D. M. Miller & C. Busby (Eds.), *Jurassic magmatism and tectonics of the North American Cordillera: Geological Society of America Special Paper* (Vol. 299, pp. 267–294). https://doi.org/10.1130/SPE299-p267

Miller, E. L., & Gans, P. B. (1989). Cretaceous crustal structure and metamorphism in the hinterland of the Sevier thrust belt, western US Cordillera. *Geology*, *17*(1), 59–62. https://doi.org/10.1130/0091-7613(1989)017<0059:ccsami>2.3.co;2

Miller, E. L., Gans, P. B., & Garing, J. (1983). The Snake Range decollement: An exhumed mid-Tertiary ductile-brittle transition. *Tectonics*, *2*(3), 239–263. https://doi.org/10.1029/tc002i003p00239

Naruk, S. J., Bykerk-Kauffman, A., Gehrels, G. E., & Spencer, J. E. (1990). Late Cretaceous and Tertiary deformation of the Santa Catalina metamorphic core complex, Arizona. *Geologic Excursions through the Sonora Desert Region, Arizona and Sonora. Arizona Geological Survey Special Paper*, *7*, 41–50.

Neumann, B. (2000). Texture development of recrystallized quartz polycrystals unraveled by orientation and misorientation characteristics. *Journal of Structural Geology*, *22*(11–12), 1695–1711. https://doi.org/10.1016/s0191-8141(00)00060-2

Okudaira, T., Takeshita, T., Hara, I., & Ando, J. I. (1995). A new estimate of the conditions for transition from basal< a> to prism [c] slip in naturally deformed quartz. *Tectonophysics*, *250*(1–3), 31–46. https://doi.org/10.1016/0040-1951(95)00039-4

Osborn, G., & Bevis, K. (2001). Glaciation in the Great Basin of the western United States. *Quaternary Science Reviews*, *20*(13), 1377–1410. https://doi.org/10.1016/s0277-3791(01)00002-6

Perkins, M. E., & Nash, B. P. (2002). Explosive silicic volcanism of the Yellowstone hotspot: The ash fall tuff record. *The Geological Society of America Bulletin*, *114*(3), 367–381. https://doi.org/10.1130/0016-7606(2002)114<0367:esvoty>2.0.co;2

Piette-Lauzière, N., Larson, K. P., Kellett, D. A., & Graziani, R. (2020). Intracrystalline vorticity record of flow kinematics during shear zone reactivation. *Journal of Structural Geology*, *140*, 104134.

Platt, J. P., Behr, W. M., & Cooper, F. J. (2015). Metamorphic core complexes: Windows into the mechanics and rheology of the crust. *Journal of the Geological Society*, *172*(1), 9–27. https://doi.org/10.1144/jgs2014-036

Ponce, D. A., Watt, J. T., & Bouligand, C. (2011). Geophysical setting of the 21 February 2008 Mw 6.0 Wells Earthquake, Nevada, implications for earthquake hazards. *Nevada Bureau of Mines and Geology Special Publication*, *36*.

Poole, F. G., & Sandberg, C. A. (1977). Mississippian paleogeography and tectonics of the western United States. In J. H. Stewart, (Eds.), *Paleozoic paleogeography of the western United States, Pacific Coast Paleogeography Symposium I* (pp. 67–85). Pacific Section, Society of Economic Paleontologists and Mineralogists.

Premo, W. R., Moscati, R. J., McGrew, A. J., & Snoke, A. W. (2014). New U-Pb zircon geochronology of Precambrian paragneisses and late Phanerozoic orthogneisses of the Angel Lake-Lizzie Basin region of the East Humboldt Range, northeastern Nevada—A comparison with the thermal chronology at Lamoille Canyon in the adjacent Ruby Mountains: Geological Society of America Abstracts with Programs, (p. 46).

Ramberg, H. (1981). The role of gravity in orogenic belts. *Geological Society, London, Special Publications*, *9*(1), 125–140.

Rehrig, W. A., & Reynolds, S. (1980). *Geologic and geochronologic reconnaissance of a northwest-trending zone of metamorphic core complexes in southern and western Arizona* (Vol. 153, pp. 131–157). Memoir of the Geological Society of America.

Rey, P. F., Mondy, L., Duclaux, G., Teyssier, C., Whitney, D. L., Bocher, M., & Prigent, C. (2017). The origin of contractional structures in extensional gneiss domes. *Geology*, *45*(3), 263–266. https://doi.org/10.1130/g38595.1

Rey, P. F., Teyssier, C., & Whitney, D. L. (2009). Extension rates, crustal melting, and core complex dynamics. *Geology*, *37*(5), 391–394. https://doi.org/10.1130/g25460a.1

Sander, B. (1930). *Gefugekunde der Gesteine*. Vienna: Springer-Verlag OHG.

Satarugsa, P., & Johnson, R. A. (2000). Cenozoic tectonic evolution of the Ruby Mountains metamorphic core complex and adjacent valleys, northeastern Nevada. *Rocky Mountain Geology*, *35*(2), 205–230. https://doi.org/10.2113/35.2.205

Saylor, J. E., & Sundell, K. E. (2016). Quantifying comparison of large detrital geochronology data sets. *Geosphere*, *12*(1), 203–220. https://doi.org/10.1130/ges01237.1

Sharp, R. P. (1939). Basin-range structure of the Ruby-East Humboldt Range, north-eastern Nevada. *Bulletin of the Geological Society of America*, *50*(6), 881–920. https://doi.org/10.1130/gsab-50-881

Sicard, K. R., & Snoke, A. W. (2021). Geologic map of the Gordon Creek quadrangle, Elko County, Nevada. *Nevada Bureau of Mines and Geology Map*, *188*, 28. 1:24,000 scale.

Simpson, C., & De Paor, D. G. (1993). Strain and kinematic analysis in general shear zones. *Journal of Structural Geology*, *15*(1), 1–20. https://doi.org/10.1016/0191-8141(93)90075-l

Skemer, P., Katayama, I., Jiang, Z., & Karato, S. I. (2005). The misorientation index: Development of a new method for calculating the strength of lattice-preferred orientation. *Tectonophysics*, *411*(1–4), 157–167. https://doi.org/10.1016/j.tecto.2005.08.023

Smith, J. F., & Ketner, K. B. (1978). *Geologic map of the Carlin-Pinon Range area* (Vol. 1028).Nevada: and Eureka Counties.

Smith, M. E., Cassel, E. J., Jicha, B. R., Singer, B. S., & Canada, A. S. (2017). Hinterland drainage closure and lake formation in response to middle Eocene Farallon slab removal, Nevada, USA. *Earth and Planetary Science Letters*, *479*, 156–169. https://doi.org/10.1016/j.epsl.2017.09.023

Snoke, A. W. (1980). Transition from infrastructure to suprastructure in the northern Ruby Mountains, Nevada. *Cordilleran metamorphic core complexes* (Vol. 153, pp. 287–333). Geological Society of America Memoir.

Snoke, A. W., Howard, K., & Dee, S. (2021). *Geologic map of the Secret Valley quadrangle, Elko County, Nevada*. Nevada Bureau of Mines and Geology Map. 1:24,000 scale.

Snoke, A. W., Howard, K. A., McGrew, A. J., Burton, B. R., Barnes, C. G., Peters, M. T., & Wright, J. E. (1997). *The grand tour of the Ruby-East Humboldt metamorphic core complex, northeastern Nevada: Part 1—Introduction & road log* (Vol. 42). Brigham Young University Geology Studies.

Snoke, A. W., McGrew, A. J., Valasek, P. A., & Smithson, S. B. (1990). A crustal cross-section for a terrain of superimposed shortening and extension: Ruby Mountains-East Humboldt Range metamorphic core complex, Nevada. In *Exposed cross-sections of the continental crust* (pp. 103–135). Dordrecht: Springer. https://doi.org/10.1007/978-94-009-0675-4_5

Snoke, A. W., & Miller, D. M. (1988). Metamorphic and tectonic history of the northeastern Great Basin. In W. G. Ernst (Eds.), *Metamorphism and crustal evolution of the western United States: Englewood Cliffs, New Jersey, Prentice Hall* (Vol. 7, pp. 606–648).

Speed, R. C., & Sleep, N. H. (1982). Antler orogeny and foreland basin: A model. *The Geological Society of America Bulletin*, *93*(9), 815–828. https://doi.org/10.1130/0016-7606(1982)93<815:aoafba>2.0.co;2

Stewart, J. H. (1972). Initial deposits in the Cordilleran geosyncline: Evidence of a Late Precambrian (<850 m.y.) continental separation. *The Geological Society of America Bulletin*, *83*, 1345–1360. https://doi.org/10.1130/0016-7606(1972)83[1345:iditcg]2.0.co;2

Stewart, J. H., & Poole, F. G. (1974). *Lower Paleozoic and uppermost Precambrian Cordilleran miogeocline, Great Basin, western United States*. Special Publications of SEPM.

Stipp, M., Stünitz, H., Heilbronner, R., & Schmid, S. M. (2002). Dynamic recrystallization of quartz: Correlation between natural and experimental conditions. *Geological Society, London, Special Publications*, *200*(1), 171–190. https://doi.org/10.1144/gsl.sp.2001.200.01.11

Sylvester, A. G., Ortel, G., Nelson, C. A., & Christie, J. M. (1978). Papoose flat pluton: A granitic blister in the Inyo Mountains, California. *The Geological Society of America Bulletin*, *89*(8), 1205–1219. https://doi.org/10.1130/0016-7606(1978)89<1205:pfpagb>2.0.co;2

Teyssier, C., Ferré, E. C., Whitney, D. L., Norlander, B., Vanderhaeghe, O., & Parkinson, D. (2005). Flow of partially molten crust and origin of detachments during collapse of the Cordilleran orogen. *Geological Society, London, Special Publications*, *245*(1), 39–64. https://doi.org/10.1144/gsl.sp.2005.245.01.03

Teyssier, C., & Whitney, D. L. (2002). Gneiss domes and orogeny. *Geology*, *30*(12), 1139–1142. https://doi.org/10.1130/0091-7613(2002)030<1139:gdao>2.0.co;2

Thorman, C. H., Ketner, K. B., Brooks, W. E., Snee, L. W., & Zimmerman, R. A. (1991). Late Mesozoic-Cenozoic tectonics in northeastern Nevada. In *Geology and ore deposits of the Great Basin. Symposium proceedings* (Vol. 1, pp. 25–45). Reno, Nevada: Geological Society of Nevada.

Thorman, C. H., Sandberg, C. A., Henry, C. D., Zuza, A. V., & Ressel, M. W. (2019). *Regional tectonics and conodont CAIs indicate normal burial depths, not Mesozoic thickening, in the Pequop Mountains*, (Vol. 51(4)). Geological Society of America, Abstracts with Programs. https://doi.org/10.1130/abs/2019CD-329504

Tokle, L., Hirth, G., & Behr, W. M. (2019). Flow laws and fabric transitions in wet quartzite. *Earth and Planetary Science Letters*, *505*, 152–161. https://doi.org/10.1016/j.epsl.2018.10.017

Toy, V. G., Prior, D. J., & Norris, R. J. (2008). Quartz fabrics in the Alpine Fault mylonites: Influence of pre-existing preferred orientations on fabric development during progressive uplift. *Journal of Structural Geology*, *30*(5), 602–621. https://doi.org/10.1016/j.jsg.2008.01.001

Tullis, J., & Yund, R. A. (1985). Dynamic recrystallization of feldspar: A mechanism for ductile shear zone formation. *Geology*, *13*(4), 238–241. https://doi.org/10.1130/0091-7613(1985)13<238:drofam>2.0.co;2

Van Buer, N. J., Miller, E. L., & Dumitru, T. A. (2009). Early Tertiary paleogeologic map of the northern Sierra Nevada batholith and the northwestern Basin and Range. *Geology*, *37*(4), 371–374. https://doi.org/10.1130/g25448a.1

Vermeesch, P. (2013). Multi-sample comparison of detrital age distributions. *Chemical Geology*, *341*, 140–146. https://doi.org/10.1016/j.chemgeo.2013.01.010

Vollmer, F. W. (1990). An application of eigenvalue methods to structural domain analysis. *The Geological Society of America Bulletin*, *102*(6), 786–791. https://doi.org/10.1130/0016-7606(1990)102<0786:aaoemt>2.3.co;2

Wallace, A. R., Perkins, M. E., & Fleck, R. J. (2008). Late Cenozoic paleogeographic evolution of northeastern Nevada: Evidence from the sedimentary basins. *Geosphere*, *4*(1), 36–74. https://doi.org/10.1130/ges00114.1

Wenk, H. R., & Wilde, W. R. (1972). *Orientation distribution diagrams for three Yule marble fabrics* (Vol. 16, pp. 83–94). Washington DC American Geophysical Union Geophysical Monograph Series.

Wernicke, B. (1981). Low-angle normal faults in the Basin and Range Province: Nappe tectonics in an extending orogen. *Nature*, *291*(5817), 645–648. https://doi.org/10.1038/291645a0

Wernicke, B., & Axen, G. J. (1988). On the role of isostasy in the evolution of normal fault systems. *Geology*, *16*(9), 848–851. https://doi.org/10.1130/0091-7613(1988)016<0848:otroii>2.3.co;2

Wesnousky, S. G., Briggs, R. W., Caffee, M. W., Ryerson, F. J., Finkel, R. C., & Owen, L. A. (2016). Terrestrial cosmogenic surface exposure dating of glacial and associated landforms in the Ruby Mountains-East Humboldt Range of central Nevada and along the northeastern flank of the Sierra Nevada. *Geomorphology*, *268*, 72–81. https://doi.org/10.1016/j.geomorph.2016.04.027

Wesnousky, S. G., & Willoughby, C. H. (2003). Neotectonic note: The Ruby-East Humboldt Range, northeastern Nevada. *Bulletin of the Seismological Society of America*, *93*(3), 1345–1354. https://doi.org/10.1785/0120020032

Whitney, D. L., Teyssier, C., Rey, P., & Buck, W. R. (2013). Continental and oceanic core complexes. *GSA Bulletin*, *125*(3–4), 273–298. https://doi.org/10.1130/b30754.1

Wickham, S. M., & Peters, M. T. (1992). Oxygen and carbon isotope profiles in metasediments from Lizzies Basin, East Humboldt Range, Nevada: Constraints on mid-crustal metamorphic and magmatic volatile fluxes. *Contributions to Mineralogy and Petrology*, *112*(1), 46–65. https://doi.org/10.1007/bf00310955

Wickham, S. M., & Peters, M. T. (1993). High δ^{13}C Neoproterozoic carbonate rocks in western North America. *Geology*, *21*(2), 165–168. https://doi.org/10.1130/0091-7613(1993)021<0165:hcncri>2.3.co;2

Wightman, R. H., Prior, D. J., & Little, T. A. (2006). Quartz veins deformed by diffusion creep-accommodated grain boundary sliding during a transient, high strain-rate event in the Southern Alps, New Zealand. *Journal of Structural Geology*, *28*(5), 902–918. https://doi.org/10.1016/j.jsg.2006.02.008

Woodcock, N. H. (1977). Specification of fabric shapes using an eigenvalue method. *The Geological Society of America Bulletin*, *88*(9), 1231–1236. https://doi.org/10.1130/0016-7606(1977)88<1231:sofsua>2.0.co;2

Wright, J. E., & Snoke, A. W. (1993). Tertiary magmatism and mylonitization in the Ruby-East Humboldt metamorphic core complex, northeastern Nevada: U-Pb geochronology and Sr, Nd, and Pb isotope geochemistry. *The Geological Society of America Bulletin*, *105*(7), 935–952. https://doi.org/10.1130/0016-7606(1993)105<0935:tmamit>2.3.co;2

Yonkee, W. A., & Weil, A. B. (2015). Tectonic evolution of the Sevier and Laramide belts within the North American Cordillera orogenic system. *Earth-Science Reviews*, *150*, 531–593. https://doi.org/10.1016/j.earscirev.2015.08.001

Zhao, N., Jr., & Cong, F. (2014). Microstructural characteristics and deformation mechanism of the shear zone of Fangshan Pluton, north China. In *AGU Fall Meeting Abstracts* (Vol. 2014, pp. T31A–4558).

Zuza, A. V., Cao, W., Hinz, N. H., DesOrmeau, J. W., Odlum, M. L., & Stockli, D. F. (2019). Footwall rotation in a regional detachment fault system: Evidence for horizontal-axis rotational flow in the Miocene Searchlight pluton, NV. *Tectonics*, *38*(7), 2506–2539. https://doi.org/10.1029/2019tc005513

Zuza, A. V., Dee, S., Hurlow, H. A., Snoke, A. W., & Laabs, B. J. C. (2021). Geologic map of the Tent Mountain quadrangle, Elko County, Nevada: Nevada Bureau of Mines and Geology Open-File Report 21, scale 1:24,000.

Zuza, A. V., Henry, C. D., Dee, S., Thorman, C. H., & Heizler, M. T. (2021). Records of pulsed intracontinental plateau growth and subsequent collapse in the North American Cordilleran hinterland: Jurassic-Cenozoic tectonics of the Pequop Mountains, NE Nevada. *Geosphere*.

Zuza, A. V., Levy, D. A., & Mulligan, S. R. (2022). Geologic field evidence for non-lithostatic overpressure recorded in the North American Cordillera hinterland, northeast Nevada. *Geoscience Frontiers*. https://doi.org/10.1016/j.gsf.2020.10.006

Zuza, A. V., Thorman, C. H., Henry, C. D., Levy, D. A., Dee, S., Long, S. P., et al. (2020). Pulsed Mesozoic Deformation in the Cordilleran Hinterland and Evolution of the Nevadaplano: Insights from the Pequop Mountains, NE Nevada. *Lithosphere*, *2020*(1). https://doi.org/10.2113/2020/8850336

References From the Supporting Information

Black, L. P., Kamo, S. L., Allen, C. M., Aleinikoff, J. N., Davis, D. W., Korsch, R. J., & Foudoulis, C. (2003). TEMORA 1: A new zircon standard for Phanerozoic U-Pb geochronology. *Chemical Geology*, *200*(1–2), 155–170. https://doi.org/10.1016/s0009-2541(03)00165-7

Gehrels, G. E., Kapp, P., DeCelles, P., Pullen, A., Blakey, R., Weislogel, A., et al. (2011). Detrital zircon geochronology of pre-Tertiary strata in the Tibetan-Himalayan orogen. *Tectonics*, *30*(5). https://doi.org/10.1029/2011tc002868

Gehrels, G. E., Valencia, V. A., & Ruiz, J. (2008). Enhanced precision, accuracy, efficiency, and spatial resolution of U-Pb ages by laser ablation-multicollector-inductively coupled plasma-mass spectrometry. *Geochemistry, Geophysics, Geosystems*, *9*(3). https://doi.org/10.1029/2007gc001805

McKinney, S. T., Cottle, J. M., & Lederer, G. W. (2015). Evaluating rare earth element (REE) mineralization mechanisms in Proterozoic gneiss, Music Valley, California. *Bulletin*, *127*(7–8), 1135–1152. https://doi.org/10.1130/b31165.1

Middlemost, E. A. (1994). Naming materials in the magma/igneous rock system. *Earth-Science Reviews*, *37*(3–4), 215–224.

Paton, C., Woodhead, J. D., Hellstrom, J. C., Hergt, J. M., Greig, A., & Maas, R. (2010). Improved laser ablation U-Pb zircon geochronology through robust downhole fractionation correction. *Geochemistry, Geophysics, Geosystems*, *11*(3). https://doi.org/10.1029/2009gc002618

Say, M., & Zuza, A. V. (2020). Late Miocene Transition between Basin and Range Extension and Walker Lane Tectonics, Northern Pine Nut Mountains, Nevada: New Insights from Geologic Mapping and 40Ar/39Ar Geochronology: Geological Society of Nevada 2020 Proceedings.

Sláma, J., Košler, J., Condon, D. J., Crowley, J. L., Gerdes, A., Hanchar, J. M., et al. (2008). Plešovice zircon—A new natural reference material for U-Pb and Hf isotopic microanalysis. *Chemical Geology*, *249*(1–2), 1–35.

Wiedenbeck, M., Hanchar, J. M., Peck, W. H., Sylvester, P., Valley, J., Whitehouse, M., et al. (2004). Further characterization of the 91,500 zircon crystal. *Geostandards and Geoanalytical Research*, *28*(1), 9–39. https://doi.org/10.1111/j.1751-908x.2004.tb01041.x

Yakymchuk, C., Kirkland, C. L., & Clark, C. (2018). Th/U ratios in metamorphic zircon. *Journal of Metamorphic Geology*, *36*(6), 715–737. https://doi.org/10.1111/jmg.12307